IL-4 induces CD22 expression to restrain the effector program of self-reactive virtual memory T cells

Benjamin Dewals (bgdewals@uliege.be)
University of Liège https://orcid.org/0000-0003-1497-0799
Bin Yang
University of Liege
Guillem Sanchez Sanchez
Université Libre de Bruxelles https://orcid.org/0000-0001-9919-1748
Arnaud Lavergne
University of Liege
Ophelie Piedfort
University of Liege
Garrie Peng
McGill University
Ariel Madrigal Aguirre
McGill University
Georgios Petrellis
University of Liege https://orcid.org/0000-0002-6444-4378
Brunette Katsandegwaza
University of Liege
Gert Van Isterdael
VIB-UGent https://orcid.org/0000-0001-6626-1316
Julie Van Duyse
VIB UGent Center for Inflammation Research
Qiang Bai
MedXCell https://orcid.org/0000-0001-7423-0712
Thomas Marichal
Liège University https://orcid.org/0000-0003-1688-6291
Bénédicte Machiels
University of Liège https://orcid.org/0000-0003-1326-3865
Lars Nitschke
Friedrich-Alexander-Universität Erlangen-Nürnberg
Hamed Najafabadi

McGill University

Irah King

McGill University Health Centre https://orcid.org/0000-0001-6990-7231

David Vermijlen

Department of Pharmacotherapy and Pharmaceutics, Université Libre de Bruxelles (ULB)
https://orcid.org/0000-0002-7605-8845

Article

Keywords:

Posted Date: April 6th, 2023

DOI: https://doi.org/10.21203/rs.3.rs-2747693/v1

Additional Declarations: There is **NO** Competing Interest.

IL-4 induces CD22 expression to restrain the effector program of self-reactive virtual memory T cells

Bin Yang[1], Guillem Sanchez-Sanchez[2,3,4,5], Arnaud Lavergne[6], Piedfort Ophélie[1], Garrie Peng[7,8,9], Ariel Madrigal Aguirre[10,11], Georgios Petrellis[1], Brunette Katsandegwaza[1], Gert van Isterdael[12,13], Julie Van Duyse[12,13], Qiang Bai[13], Thomas Marichal[5,14], Bénédicte Machiels[1], Lars Nitschke[15], Hamed S. Najafabadi[10,11], Irah L. King[7,8,9], David Vermijlen[2,3,4,5], Benjamin G. Dewals[1,*]

[1]Department of Infectious and Parasitic Diseases, Faculty of Veterinary Medicine – FARAH, University of Liège, Liège, Belgium.
[2]Department of Pharmacotherapy and Pharmaceutics, Université Libre de Bruxelles (ULB), Brussels, Belgium
[3]Institute for Medical Immunology (IMI), Université Libre de Bruxelles (ULB), Gosselies, Belgium.
[4]ULB Center for Research in Immunology (U-CRI), Belgium.
[5]WELBIO Department, WEL Research Institute, Wavre, Belgium
[6]GIGA-Genomics core facility, University of Liège, Liège, Belgium
[7]Department of Microbiology and Immunology, Meakins-Christie Laboratories, Research Institute of McGill University Health Centre, Montreal, Quebec, Canada
[8]McGill Interdisciplinary Initiative in Infection and Immunity, Montreal, Quebec, Canada
[9]McGill Centre for Microbiome Research, Montreal, Quebec, Canada
[10]Department of Human Genetics, McGill University, Montreal, QC, H3A 0C7, Canada
[11]McGill Genome Centre, Dahdaleh Institute of Genomic Medicine, Montreal, QC, H3A 0G1, Canada
[12]VIB Flow Core, VIB Center for Inflammation Research, Ghent, Belgium
[13]Department of Biomedical Molecular Biology, Ghent University, Ghent, Belgium.
[14]Laboratory of Immunophysiology, GIGA Institute, ULiège, Liège, Belgium
[15]Division of Genetics, Department of Biology, University of Erlangen, 91058 Erlangen, Germany

*corresponding author: bgdewals@uliege.be

Abstract

Parasitic helminths induce the production of interleukin (IL)-4 which causes the expansion of virtual memory $CD8^+$ T cells (T_{VM}), a cell subset contributing to the control of viral coinfection. However, the mechanisms regulating IL-4-dependent T_{VM} activation and expansion during worm infection remain ill defined. We used single-cell RNA sequencing of $CD8^+$ T cells to investigate IL-4-dependent T_{VM} responses upon helminth infection in mice. Gene signature analysis of $CD8^+$ T cells identified a cell cluster marked by CD22, a canonical regulator of B cell activation, as a specific and selective surface marker of IL-4-induced T_{VM} cells. $CD22^+$ T_{VM} were enriched for IFN-γ and granzyme A and retained a diverse TCR repertoire, while enriched in CDR3 sequences with features of self-reactivity. Deletion of CD22 expression in $CD8^+$ T cells enhanced T_{VM} responses to helminth infection, indicating that this inhibitory receptor modulates T_{VM} responses. Thus, helminth-induced IL-4 drives the expansion and activation of self-reactive T_{VM} in the periphery that is counter-inhibited by CD22.

Introduction

Helminths are widespread parasitic worms responsible for the infection of about a quarter of the human population[1]. In high burden infections, helminths can induce debilitating and chronic disease with a strong impact on health and welfare[2,3]. However, most helminth infections are of low burden, with a limited number of parasites persisting in their host for several months and even years. Worm persistence can be explained by a finely regulated balance between immune control and evasion to tolerate the parasites, while avoiding critical harm[4,5]. Helminths generally induce robust and protective type 2 immunity, which is characterized by the production of type 2 cytokines including interleukin (IL)-4, IL-5, and IL-13. Type 2 cytokines are produced by and activate key immune cells such as group 2 innate lymphoid cells (ILC2s), eosinophils, mast cells, macrophages and $CD4^+$ T helper 2 (Th2) cells, which coordinate immune protection[5]. In addition to these effector mechanisms, helminth infection also induces the expansion of a specific population of memory-phenotype $CD8^+$ T cells in the secondary lymphoid organs that are referred to as virtual memory T cells (T_{VM})[6–9].

T_{VM} have many characteristics in common with true memory $CD8^+$ T cells (T_{TM}), which arise in the periphery in response to a foreign antigen and are characterized by their ability to develop fast and effective responses after repeated encounters with the same antigen[10]. Likewise, T_{VM} can also rapidly respond in the early phase of infection with pathogens[11–14]. However, in contrast to T_{TM}, T_{VM} have the particularity to differentiate and develop in absence of foreign antigen[13,15,16]. In naive conditions, T_{VM} are $CD8^+$ αβ T cells that are found in substantial proportions in conventionally housed mice, as well as in germ-free (GF) mice[17]. While T_{VM} exhibit a $CD44^{hi}CD122^+CXCR3^{hi}$ memory phenotype, they differ from T_{TM} since they downregulate the α4 integrin (*Itga4*, CD49d), which is normally upregulated in response to TCR activation[18]. T_{VM} have been described in human, but there is still a significant lack of specific markers to distinguish them from T_{TM}, in both human and mice[16,19–21]. The developmental origin of the memory phenotype of T_{VM} has been recently explained by the recognition of self-ligands during maturation in the thymus, driving the upregulation of the transcription factor eomesodermin (EOMES) in T cell precursors[17,22]. In addition to self-specificity, T_{VM} differentiation in the thymus and expansion in the periphery also requires signals from IL-4 and/or IL-15, depending on the mouse strain[8,23–26]. Invariant natural killer T cells produce IL-4 in BALB/c mice[24,27], driving memory-phenotype T cell differentiation in the thymus. In addition, IL-4 signaling is also required in the periphery to maintain T_{VM} in this strain[6,25]. In contrast, C57BL/6 mice seem to mainly rely on IL-15 for T_{VM} differentiation and maintenance at steady-state[8,21,26,28]. Efforts have been made to decipher the function of T_{VM} in homeostasis as well as in response to infection or tumor development [6,7,17,29,30], but the

regulation of helminth-induced T_{VM} remains unclear. T_{VM} significantly expand in the periphery during helminth infection, but the role of IL-4 and IL-15 in this expansion is controversial and/or redundant, irrespective of the mouse strain[6,7,9,29]. Nevertheless, expansion of T_{VM} after helminth infection can result in enhanced $CD8^+$ T cell-mediated control against bystander viral coinfection[6], which was also observed in bacterial coinfection[7]. Thus, the increased numbers of T_{VM} in helminth infection can drive protection against concurrent intracellular pathogens. However, the mechanisms regulating T_{VM} expansion during helminth infection remain incompletely defined.

Here, we addressed this important question by studying IL-4 signaling and consequences in the circulating $CD8^+$ T cell population during helminth infection. We employed single-cell RNA sequencing (scRNA-seq) to investigate transcriptomic gene signatures and interrogate cellular heterogeneity to identify unique features of IL-4-induced T_{VM}. Our findings identified a specialized program of differentiation instructed by IL-4 in T_{VM}, including the unanticipated upregulation of CD22, a canonical inhibitory receptor of B lymphocytes. CD22 was upregulated in IL-4-induced self-reactive T_{VM} specifically and the absence of CD22 resulted in an enhanced T_{VM} response to IL-4 during helminth infection.

Results

Required IL-4Rα expression on peripheral CD8$^+$ T cells for T_{VM} maintenance. In BALB/c mice, IL-4 is required for the differentiation of unconventional memory T cell in both the thymus and the periphery[6,27]. To study IL-4-mediated T_{VM} expansion in the periphery, a BALB/c mouse model was generated in which peripheral CD8$^+$ T lymphocytes have impaired expression of the IL-4 receptor α chain (IL-4Rα). Specifically, *E8i^{Cre}* C57BL/6 mice were backcrossed for 9 generations with *Il4ra$^{lox/lox}$* BALB/c mice (WT) to generate IL-4Rα$^{\Delta CD8}$ BALB/c mice. In *E8i^{Cre}* mice, Cre expression is driven through the control of an E8i-CD8α enhancer/promoter construct[31]. The enhancer E8i is activated in maturating single positive CD8$^+$ T lymphocytes (SP8) before exiting the thymus to the periphery. In naive conditions, single positive CD4$^+$ (SP4) and SP8 expressed similar levels of IL-4Rα (CD124) in both WT and IL-4Rα$^{\Delta CD8}$ mice (**Fig. 1a**). However, a small subset of CD24$^-$ SP8 cells in which E8i enhancer is activated[32], start to lose CD124 expression in IL-4Rα$^{\Delta CD8}$ mice (**Fig. 1b**). As expected, splenic CD3$^+$CD8$^+$ T cells expressed significantly lower levels of CD124 (**Fig. 1c**), whereas CD3$^+$CD8$^-$ T cells and other cell types retain high CD124 expression in IL-4Rα$^{\Delta CD8}$ mice (**Fig. 1c**, **Extended Data Fig. 1a**). T_{VM} were gated as CD44^{hi}CXCR3$^+$CD49d^{low}CD3$^+$CD8$^+$ T cells (**Extended Data Fig. 1b**), and IL-4Rα$^{\Delta CD8}$ mice had significantly less T_{VM} when compared to WT littermate controls (**Fig. 1d**). These results support previous observations regarding the IL-4Rα requirement for peripheral T_{VM} differentiation[6,25] and further demonstrate that IL-4 significantly contributes to T_{VM} maintenance in the periphery in naive conditions. However, a population of T_{VM} retained the expression of CD124 in IL-4Rα$^{\Delta CD8}$ mice (**Fig. 1e**), suggesting incomplete deletion of *Il4ra* in IL-4Rα$^{\Delta CD8}$ (**Fig. 1f and Extended Data Fig. 1c-d**). Thus, peripheral IL-4 signaling is required for T_{VM} maintenance, and IL-4Rα$^{\Delta CD8}$ mice are partial knockout in which the remaining T_{VM} population mainly arises from IL-4Rα-expressing CD8$^+$ T cells, likely escaping genetic deletion driven by the *E8i^{Cre}* transgene.

T_{VM} expansion is reduced in IL-4Rα$^{\Delta CD8}$ mice after IL-4c treatment and helminth exposure. During helminth infection, IL-4 can expand T_{VM}[6,7]. To study the effect of IL-4 signaling on peripheral CD8$^+$ T cells, IL-4Rα$^{\Delta CD8}$ and WT littermate control mice were treated with recombinant IL-4 complexed with a monoclonal antibody to IL-4 (IL-4c), which extends the bioactive half-life of the cytokine and artificially induces an IL-4 dominant environment (**Fig. 1g-i**). We found that although maturating thymic CD24$^-$ SP8 started to lose CD124 and IL-4c upregulated expression of the transcription factor eomesodermin (EOMES) in SP8, there were no significant difference in CD24$^-$ SP8 proportions or EOMES expression between WT and IL-4Rα$^{\Delta CD8}$ mice (**Fig. 1g**). In the spleen, IL-4c induced the expansion of T_{VM} and upregulated the expression of EOMES in WT mice, while T_{VM} expansion and EOMES expression levels were

reduced in IL-4Rα$^{\Delta CD8}$ mice (**Fig. 1h**), confirming significant deletion of the *Il4ra* locus. However, IL-4c treatment increased the proportions of CD124^{+} CD8^{+} T cells in IL-4Rα$^{\Delta CD8}$ mice (**Fig. 1i**), likely through selection of cells retaining IL-4Rα expression. When focusing on CXCR3^{+} T_{VM}, we found that although significantly reduced compared to WT controls, a significant proportion of CXCR3^{+} cells was still present in IL-4Rα$^{\Delta CD8}$ animals. However, the majority of CXCR3^{+} T_{VM} cells retained surface expression of CD124, confirming that IL-4Rα$^{\Delta CD8}$ mice are partial knockout mice for *Il4ra* locus (**Extended Data Fig. 1e**). We further explored T_{VM} expansion in IL-4Rα$^{\Delta CD8}$ mice exposed to helminths using injection of *S. mansoni* eggs or infected with the gastro-intestinal nematode *Heligmosomoides polygyrus*. A significant reduction of T_{VM} expansion was observed in IL-4Rα$^{\Delta CD8}$ mice (**Fig. 1j**). Importantly, expansion of T_{VM} during helminth infection required IL-4Rα expression by CD8^{+} T cells, since the majority of T_{VM} in IL-4Rα$^{\Delta CD8}$ mice were found in the CD124^{+} compartment but significantly lower in CD124^{-} T cells (**Fig. 1k**). However, *H. polygyrus* infection was not affected in IL-4Rα$^{\Delta CD8}$ mice as attested by similar worm burden at day 15 after infection (**Fig. 1l**). Together, these data demonstrate that during helminth infection IL-4 directly induces T_{VM} expansion in peripheral CD8^{+} T cells, impaired in IL-4Rα$^{\Delta CD8}$ mice.

Single-cell transcriptomic analysis reveals peripheral T_{VM} signature. To investigate the transcriptomic program of CD8^{+} T cell responses to IL-4 during helminth infection, single-cell RNA-seq (scRNA-seq) was performed on CD8^{+} T cells enriched from the spleen of IL-4Rα$^{\Delta CD8}$ and littermate control WT mice after IL-4c treatment or *H. polygyrus* infection (**Extended Data Fig. 2a**). Doublets and contaminating non-CD8^{+} T cells were excluded (exclusion of cells expressing *Cd19, Cd4, Ncr1, Itgax, Tcrg-C1, Tcrg-C3, Tcrg-C4, Trdc*) and a total of 33,553 cells were analysed in which ~30-50,000 reads and ~2,000 genes per cell were detected. Six datasets were obtained based on the treatment (PBS, IL-4c and *H. polygyrus*) and genotype (IL-4Rα$^{\Delta CD8}$ and littermate WT control). Clustering on the Uniform Manifold Approximation and Projection (UMAP) representation identified 17 distinct clusters (**Fig. 2a, Extended Data Fig. 2b-c**). Hash tagging allowed separation of cells from individual mice in each dataset to visualize the proportional dispersion of each cluster for each individual mouse (**Extended Data Fig. 2d**). Based on gene signatures and increased proportions upon IL-4 response, cluster 6 was identified as the cluster in which T_{VM} would be most likely found as memory genes were upregulated and *Itga4* downregulated (**Extended Data Fig. 2d-f**). To better define the T_{VM} population, SingleR analysis was performed on the same merged datasets to identify naive, memory and effector T cells based on signature genes (**Fig. 2b-c**)[33]. Cells having a signature of memory or effector T cells were then extracted from the main object and re-analysed with Seurat for clustering (**Fig. 2d-e, Extended Data Fig. 3a-b**). In total 15 clusters were identified, and differential gene expression was performed to furtherly characterize the new clusters. We

could identify Cluster 14 as terminally effector T cells (*Zeb2, Klrg1, Cx3cr1, Bhlhe40, Gzmb*), while Cluster 1 contained cells upregulating *Gzmm*. Cluster 3 and 4 upregulated genes associated with true memory (*Itga4, Gzmk, Ccl5, Cxcr3)*. Cluster 5 contained cells upregulating *Cd226, Lef1, Ccr9* and *Foxp1.* While cluster 6 upregulated *Ccr7, Il7r* and *Tcf7* and likely includes central memory T cells, the exhaustion gene *Tox* and *Lag3* were differentially upregulated in Cluster 8. Signature genes reminiscent of mucosal associated invariant T cells and/or γδ T cells such as *Cd160*, *Klra7* and *Klrc1*, as well as *Trg-C1*, *Trg-C1* were found in Cluster 9. In addition, *Cd69, Cd83, Icam1* grouped potential tissue resident T cells in Cluster 10, and interferon stimulated genes (*Isg15, Ifit1, Ifit3, Oasl1, Usp18*) were up in Cluster 11. Cluster 12 contained cells in active division potentially representing stem-like memory T cells upregulating *Mki67, Birk5, Ccnb2, Ccna2,* and *Cdk1*. Finally, cluster 2 had a gene signature related to T_{VM}, characterized by the reduced expression of *Itga4* combined with the upregulation of memory/effector genes like *Eomes*, *Ctla2a*, *Ccr2*, *Ccr5*, *Il2rb* and *Gzma* (**Fig. 2d-f**). Confirming that cluster 2 represents T_{VM}, the proportion of cells in cluster 2 was increased upon IL-4c or *H. polygyrus* infection in littermate WT control mice, while less abundant in IL-4Rα$^{\Delta CD8}$ mice (**Extended Data Fig. 3c-d**).

IL-4-induced T_{VM} upregulate signature genes including *Cd22* during helminth infection. When looking at the effects of treatment and genotype, we observed that IL-4c and *H. polygyrus* infection induced an enrichment of cells having a gene signature of memory T cells with upregulation of *Eomes*, *Cxcr3* and *Il4ra* and reduced *Itga4* (**Fig. 3a-b**). Although there was no significant difference between IL-4Rα$^{\Delta CD8}$ and littermate WT controls, likely due to the partial deletion of *Il4ra* in IL-4Rα$^{\Delta CD8}$, we observed that IL-4c treatment or *H. polygyrus* infection had a more limited effect on the expansion of memory T cells and signature gene expression levels in these mice. Trajectory pathway analysis using RNA velocity[34] showed main trajectories of differentiation from cluster 0 to clusters 1 and 2, then to cluster 4, 3 and 14 irrespective of the treatment (**Extended Data Fig. 4a**). These data suggest that T_{VM} cluster 2 originates from memory cluster 0 and that the main pathway of T_{VM} differentiation are conserved upon IL-4 activation. Interestingly, gene set enrichment analyses of individual clusters for regulation of transcription identified *Atf6* and *Cebpd* among the top enriched transcription program in response to IL-4c and *H. polygyrus*, suggesting increased cellular stress in cluster 2 (**Extended Data Fig. 4b**). Then, focusing on the differential gene expression in cluster 2 in response to both IL-4c or *H. polygyrus* infection, we observed a significant upregulation of *Gzma*, *Gzmm*, *Ctla2a, Xcl1, Bcl11b, Fyn, Ccr2, Ccr5* and *Cd22*, whereas *S1pr1, Cd55, Ly6c1, Ly6c2 and Itgb7* were downregulated (**Fig. 3c-d**). Interestingly, most of the regulated genes were also similarly regulated in data obtained by RNA sequencing on sorted T_{VM} from mice exposed to *S. mansoni* eggs (**Extended Data Fig. 4c**)[6], CD5^{+} or CD5^{-} T_{VM}[35], and CCR2^{+} T_{VM}[14],

further supporting that cluster 2 are T_{VM}. Moreover, differential gene expression analysis in cluster 2 upon IL-4c treatment and at day 15 after helminth infection confirmed the significant increased expression of *Gzma*, *Gzmm*, *Ccr5*, *Xcl1* and *Cd22* (**Fig. 3e**). At day 15 after *H. polygyrus* infection, although frequencies of T_{VM} increased in the spleen (**Fig. 4a**), a most severe expansion of T_{VM} was found in the mesenteric LN (mesLN) (**Fig. 4b**), where a significant IL-4Rα-dependent upregulation of EOMES in $CD8^+$ T cells could be observed (**Fig. 4c**). To further determine the IL-4Rα-dependent T_{VM} gene signature in the mesLN after *H. polygyrus* infection, we took advantage of the partial deletion of the *Il4ra* locus in IL-4Rα$^{\Delta CD8}$ mice. $CD124^+$ and $CD124^-$ $CD8^+$ T cells were FACSorted from the mesLN at day 15 after *H. polyygyrus* infection of IL-4Rα$^{\Delta CD8}$ mice to tag each cell population before re-pooling them and further proceed to scRNA-seq (**Fig. 4d, Extended Data Fig. 4d**). A total of 6,808 cells were validated with ~60% $CD124^+$ and ~40% $CD124^-$ cells. In $CD124^+$ cells specifically, Seurat analysis undoubtedly identified cluster 5 as IL-4-induced T_{VM} based on the upregulation of *Eomes, Il2rb, Cxcr3, Gzma, Ccr2, Ccr5,* and *Cd22* but low expression of *Itga4,* and revealed an absence of upregulation of *Gzmb* or exhaustion markers like *Pdcd1* (**Fig. 4e-f, Extended Data Fig. 4d**). Thus, these results specifically identified the nature of transcriptional changes in IL-4-induced T_{VM} during helminth infection.

CD22 expression is restricted to IL-4-induced T_{VM} cells. CD22 expression is largely restricted to B cells[36,37]. While CD22 has recently been shown to regulate other cell types such as microglia[38], the role of CD22 in T lymphocytes remains poorly defined[39,40]. *Cd22* RNA expression was mainly restricted to the T_{VM} clusters in the spleen of mice treated with IL-4c or infected with *H. polygyrus* (**Fig. 3c-d and Fig. 5a**), and in the mesLN of *H. polygyrus* infected mice (**Fig. 4e-g**). However, scRNA-seq barely detected *Cd22* expression in naive T cells (**Fig. 3d**). This observation was confirmed by immunostaining for surface CD22 where a significant proportion of $CD22^+$ cells could be detected by flow cytometry on $CD8^+$ T lymphocytes after IL-4c treatment and *H. polygyrus* infection (**Fig. 5b**). We could confirm the specific expression of CD22 by $CD8^+$ T cells by ImageStream (**Fig. 5c**), excluding any artefact due to potential cell doublets. Flow cytometry analysis of $CD22^+CD8^+$ T cells confirmed that IL-4-induced $CD22^+CD8^+$ T cells mainly express T_{VM} markers (**Fig. 5d**), further suggesting that CD22 expression is induced in T_{VM} through IL-4 signaling. Indeed, the expansion of $CD22^+$ T_{VM} by IL-4c and *H. polygyrus* infection was significantly reduced in IL-4Rα$^{\Delta CD8}$ mice (**Fig. 5e-f**). Following concatenation of flow data from multicolor staining of $CD8^+$ T cells, FlowSOM unbiased clustering analysis was performed. These analyses identified cluster C0 as being T_{VM} cells expressing high levels of CD44, CXCR3 and CD22 but lower levels of CD49d (**Extended Data Fig. 5a-b**). Importantly, cluster C0 also expressed high levels of CD124, suggesting that IL-4 signaling in T_{VM} drives CD22 expression, which was further confirmed as

CD22 was only expressed by the Cre recombinase-escaping CD124$^+$ T cells in IL-4Rα$^{\Delta CD8}$ mice, whereas CD22$^+$ cells could not be detected in CD124$^-$ T cells (**Fig. 5g, Extended Data Fig. 5c**). In addition, expansion of CD22$^+$ T cells was not observed in CD4$^+$ T cells after helminth infection (**Extended Data Fig. 5d**). Interestingly, CD22$^+$ T_{VM} strikingly expanded in the mesenteric LN (mesLN) at day 15 after worm infection and were restricted to CD124$^+$ CD8$^+$ T cells (**Fig. 5h**)**,** and upregulated EOMES (**Extended Data Fig. 5e**). Although IL-4 was shown to be required for T_{VM} maintenance in BALB/c mice, we could also observe a strong expansion of CD22$^+$ T_{VM} after IL-4c treatment or *H. polygyrus* infection of C57BL/6 mice (**Extended Data Fig. 5f**). Moreover, CD22$^+$ T_{VM} was observed in the spleen, the mesLN but also in the inguinal LN and bone marrow after *H. polygyrus* infection (**Extended Data Fig. 5f-h**), suggesting a systemic effect of IL-4 during worm infection. However, whereas T_{VM} expansion was maintained after a single injection of IL-4c, surface CD22 was transient (**Extended Data Fig. 5i**). Importantly, IL-4c treatment could not induce CD22 expression on thymic SP8 cells (**Extended Data Fig. 5j**), or on virus-specific effector T cells at 30 days after murid gammaherpesvirus 4 (MuHV-4) infection (**Extended Data Fig. 5k**). Finally, we could not detect any significant expression of CD22 on CD8$^+$ T cells from IL-4c treated or *H. polygyrus*-infected BALB/c or C57BL/6 *Il4ra*$^{-/-}$, or C57BL/6 *Stat6*$^{-/-}$ mice (**Fig. 5i**). Similarly, CD22 expression was not increased on *Il4ra*$^{-/-}$ CD8$^+$ T cells from WT:*Il4ra*$^{-/-}$ mixed bone marrow chimeras treated with IL-4c or infected with *H. polygyrus* (**Fig. 5j**). These data collectively demonstrate that CD22 is specifically upregulated by IL-4 in expanding T_{VM}.

CD22$^+$ T_{VM} induced by IL-4 display an activated phenotype. T_{VM} expressing CD22 at their surface in response to IL-4 could have a specific functional program. Thus, an in-depth transcriptomic comparative analysis by RNA-seq was performed on FACS-sorted CD44^{low} T_{NAIVE}, CD22$^+$, and CD22$^-$ CD44^{hi}CD49^{low} T_{VM} populations from PBS- or IL-4c-treated mice. Principal component analysis (PCA) revealed clustering of each analyzed cell population, suggesting that the surface expression of CD22 in T_{VM} is associated with phenotypic changes (**Extended Data Fig. 6a**). Among genes upregulated in CD22$^+$ T_{VM}, we observed upregulation of *Cd22,* as well as genes related to effector functions and activation such as *Gzma*, *Ifng*, *Eomes, Il2rb*, *Mki67, Ctla2a, Slc16a2, Gzmm, Xcl1, Ccl4, Cxcr3, Ccr2* or *Ccr5* (**Fig. 6a-b)**. Interestingly, we observed significant gene set enrichment in CD22$^+$ T_{VM} of T cell signaling, cell cycle, NK mediated killing, and IL-2/STAT5 signaling (**Fig. 6c**), as well as MAPK and BCR signaling (**Extended Data Fig. 6b**). Moreover, *Cd22* was the only upregulated siglec gene (**Extended Data Fig. 6c**), whereas genes related to T cell exhaustion such as *Pdcd1*, *Lag3*, *Havcr2* (TIM3)*, Ctla4* or *Tox* were not significantly upregulated, apart from *Tigit* (**Extended Data Fig. 6d**). In comparison to CD22$^-$ T_{VM}, CD22$^+$ T_{VM} significantly upregulated inhibitory receptors such as, *Entpd1* (CD39), *Cd160, Klra3* (Ly49c), *Klra5* (Ly49e)*, Klra7* (Ly49g), *Klrc1*

and *Klrd1* (NKG2A/CD94) and downregulated *Klrg1* and *Itga4* (CD49d) (**Fig. 6d, Extended Data Fig. 6e**). Interestingly, similar gene signatures with upregulation of *Cd22* together with its known interacting factors *Ptpn6*, *Grb2* and *Lyn*-related *Fyn* as well as upregulation of *Entpd1* or *Klra3* could be identified in the T_{VM} cluster in the mesLN during *H. polygyrus* infection (**Extended Data Fig. 6f**), suggesting that a common regulation program occurs in T_{VM} in both spleen and mesLN in response to IL-4 and during *H. polygyrus* infection. Importantly, the observed upregulation of EOMES, GZMA, CD39, CCR2, and CD160 were further confirmed by flow cytometry after IL-4c in the spleen (**Fig. 6e**) or at 2 weeks post-infection with *H. polygyrus* (**Extended Data Fig. 7a**). Moreover, $CD22^+$ T_{VM} were shown to be the main population of $CD8^+$ T cells producing IFN-γ upon IL-4 stimulation using an IFN-γ reporter mouse model (**Fig. 6f-g**). During *H. polygyrus* infection, IL-4 signaling via STAT6 activation was further demonstrated to specifically drive the expansion of peripheral T_{VM} upregulating CD22, CD39 and GZMA (**Extended Data Fig. 7b-d**). Whereas T_{VM} exist in germ-free (GF) mice[17], microbiota might contribute to CD22 upregulation. However, expansion of T_{VM} co-expressing CD22, CD39 and GZMA also occurred in GF mice infected with axenic *H. polygyrus*, demonstrating that microbiota is not critical for $CD22^+$ T_{VM} expansion (**Extended Data Fig. 7e**). Moreover, an increase in the frequency of $GATA3^+$ Th2 cells in the mesLN of mice infected with *H. polygyrus* under GF conditions was associated with an increase in CD39 and GZMA expression by $CD22^+$ T_{VM} (**Extended Data Fig. 7f**). Taken together, these data suggest that $CD22^+$ T_{VM} display an activated phenotype and that the magnitude of *in vivo* IL-4 signals is a determinant of $CD22^+$ T_{VM} activation.

$CD22^+$ T_{VM} cells possess a diverse TCR repertoire enriched in self-reactive signatures. T_{VM} mainly arise from a pool of $CD8^+$ thymocytes that display reactivity towards endogenous self-ligands[41,42]. Thus, we hypothesized that the IL-4 driven expression of the inhibitory molecule CD22 on peripheral T_{VM} cells could be restricted to self-reactive cells. In line with this, we observed an increased expression in $CD22^+$ T_{VM} of *Cd5* which is associated to self-antigen recognition[43,44] (**Fig. 6d**). Additionally, analysis of a public RNA-seq dataset revealed that $CD5^+$ T_{VM} also upregulate *Cd22*[35] (**Fig. 7a**), which was similarly found to be upregulated in $CCR2^+$ T_{VM}[14]. To investigate whether self-reactive T_{VM} could be preferentially expanded upon IL-4 signaling and whether CD22 could mark highly self-reactive TCRs, TCR sequencing was performed on $CD44^{low}$ T_{NAIVE}, $CD22^+$ T_{VM}, and $CD22^-$ T_{VM} populations from PBS- or IL-4c-treated mice (**Extended Data Fig. 8a**). Both $CD22^-$ and $CD22^+$ T_{VM} possessed a highly diverse TCR repertoire, indicating a polyclonal expansion (**Fig. 7b-c, Extended Data Fig. 8b**). To verify whether this polyclonal expansion was stochastic or whether self-reactive TCRs were favored, CDR3α and CDR3β amino acid composition was further analyzed for several key physicochemical features described to influence self-antigen recognition[45–47]. CDR3

sequences from IL-4-induced T_{VM}, especially the $CD22^+$ subset, displayed significantly enriched hydrophobic doublets in positions 6 and 7 (**Fig. 7d-e**), were enriched for CDR3 strength and volume, and showed reduced CDR3 polarity (**Fig. 7f-g and Extended Data Fig. 8c-h**). Cumulative contribution of these and additional CDR3 features were assessed by principal component analysis and revealed a significant separation of $CD22^+$ T_{VM} from other groups (**Fig. 7h and Extended Data Fig. 8i**). Supporting the hypothesis that CD22 expression is restricted to self-reactive TCR populations, IL-4c treatment induced strong T_{VM} expansion and CD22 expression in OT-I TCRtg cells, which are reported to exhibit relatively high levels of autoreactivity (**Fig. 7i**)[22,48,49]. Conversely, T_{VM} expansion and CD22 expression were significantly reduced in the non-autoreactive CSP TCRtg mice[50] after IL-4c treatment (**Fig. 7i**). Collectively, these data demonstrate that IL-4 drives the expression of CD22 at the surface of expanding self-reactive T_{VM} cells.

The lack of CD22 leads to increased activation of T_{VM} during helminth infection. The expression of the inhibitory receptor CD22 on the most self-reactive T_{VM} might contribute to counter self-peptide activation and autoimmunity. Thus, we studied T_{VM} expansion during helminth infection in CD22-deficient mice (*Cd22*$^{-/-}$)[51]. *H. polygyrus* effectively established intestinal infection in germline CD22-deficient mice (*Cd22*$^{-/-}$), with no difference of adult worm burden (**Fig. 8a**), and similar number of fecal egg counts when compared to WT C57BL/6 mice (**Fig. 8b**). Whereas $CD22^+$ T_{VM} could not be found in *Cd22*$^{-/-}$ mice, they strongly expanded in spleen and mesLN of WT mice after *H. polygyrus* infection (**Fig. 8c**). Interestingly, *Cd22*$^{-/-}$ mice had significantly more T_{VM} at steady-state and after IL-4c when compared to littermate WT mice (**Fig. 8d**). However, *H. polygyrus* infection did not affect the expansion of T_{VM} in absence of CD22 expression globally (**Fig. 8d**). Since CD22 is strongly expressed in B lymphocytes to regulate B cell responses, the absence of CD22 expression on B cells in *Cd22*$^{-/-}$ mice could indirectly interfere with T_{VM} expansion. To control for this confounding factor, mixed bone marrow WT:*Cd22*$^{-/-}$ chimeras were generated to investigate how the lack of CD22 could impact the T_{VM} response to helminth infection in a cell-intrinsic manner (**Fig. 8e**). EOMES expression levels were similarly increased in both WT and *Cd22*$^{-/-}$ donor compartments, suggesting the initial T_{VM} activation by IL-4 is not altered by the absence of CD22. However, the inability to induce CD22 expression upon IL-4c and after *H. polygyrus* infection in *Cd22*$^{-/-}$ T_{VM} resulted in significantly increased GZMA and CD39 (**Fig. 8e-f**). Importantly, T_{VM} expansion upon IL-4c treatment or *H. polygyrus* infection was also more pronounced in *Cd22*$^{-/-}$ $CD8^+$ T cell compartment (**Fig. 8f**), and the lack of CD22 resulted in significantly increased IFN-γ as well as GZMA production by $CD8^+$ T cells upon *ex vivo* restimulation (**Fig. 8g**). Thus, these data demonstrate that CD22 expression on $CD8^+$ T cells

363 counter-inhibits T_{VM} expansion and reduces the degree of T_{VM} activation during helminth
364 infection.

Discussion

Overall, our results reveal the unexpected finding that CD22 is specifically expressed by IL-4-driven self-specific T_{VM} to control their expansion and activation during helminth infection. Specifically, we have demonstrated that IL-4 signaling during *H. polygyrus* infection in peripheral $CD8^+$ T cells drives the engagement of a specific gene signature program of activation, together with CD22 and other counter-inhibitory receptors that are not related to T cell exhaustion.

We found that IL-4R$\alpha^{\Delta CD8}$ mice had significantly reduced T_{VM} population in the spleen, whereas CD124 expression was not affected in the thymus, demonstrating the selective expression of the Cre in mature $CD8^+$ T cells exiting the thymus and the requirement of IL-4 signaling in $CD8^+$ T cells to drive the expansion and functional changes in peripheral T_{VM}. Indeed, T_{VM} expansion and upregulation of signature markers of IL-4-induced T_{VM} like CD22, CD39, GZMA were specifically found in $CD124^+$ T_{VM} after *H. polygyrus* infection. Moreover, we could not observe the upregulation of these markers in *Il4ra*$^{-/-}$ or in *Stat6*$^{-/-}$ mice, irrespective of the strain background. These findings clearly highlight the requirement of IL-4 signaling in driving a specific program in T_{VM} upon helminth infection. These findings are important as IL-15 signaling has also been shown to expand T_{VM} upon *H. polygyrus* infection[9]. As both cytokines signal through the common gamma chain (γc), they might trigger overlapping intracellular activation pathways in T_{VM}[52].

The heterogeneity of the gene expression program in splenic $CD8^+$ T cells in response to IL-4c and *H. polygyrus* infection was revealed by scRNA-seq. Given the remarkable expansion of T_{VM} during helminth infection, our study enhanced the interrogation of this subset, thereby adding to our understanding of memory/effector $CD8^+$ T cell diversity previously reported using scRNA-seq approaches in other settings[53,54]. Further, gene signature analyses highlighted that T_{VM} differ from classical T_{TM} or exhausted T cells and are rather characterized by a unique combination of *Eomes*, *Il2rb*, *Ctla2a*, *Gzma*, *Gzmm, Ccr2, Ccr5,* and *Itm2a* expression. While confirming previous transcriptomic characterizations of T_{VM}[6,14,21], our scRNA-seq data suggests similar trajectories of differentiation by IL-4 or *H. polygyrus*-induced T_{VM}, and further provides unique information about the expanding T_{VM} subset. Although we also observed changes in the expression of these signature genes in IL-4R$\alpha^{\Delta CD8}$, the magnitude of their differential expression was overall reduced when compared to WT littermate controls in the spleen, likely because IL-4R$\alpha^{\Delta CD8}$ are partially knockout and a remaining population of $CD124^+CD8^+$ T cells exist. Indeed, when single cell transcriptomes were studied in sorted $CD124^+$ or $CD124^-$ $CD8^+$ T cells from the mesLN of *H. polygyrus* infected mice, IL-4-induced

T_{VM} signature was only found in IL-4Rα-competent cells. When computing the significant differentially expressed genes in both IL-4 and *H. polygyrus*-induced T_{VM}, effector genes *Gzma*, *Gzmm, Ctla2a, Ccr2* and *Ccr5* were upregulated, but we also unexpectedly observed the upregulation of *Cd22*. CD22 is a canonical inhibitory receptor of B lymphocytes which contributes to control autoimmune disease[36], and its expression on other cell types has only been scarcely reported[38–40,55]. CD22 is upregulated by microglia in aging brains, where it inhibits phagocytosis[38], and one report identified functional CD22 in primary T cells but with a very low surface expression level[39]. Interestingly, CD22 was the only sialic acid-binding immunoglobulin-type lectin (siglec) gene upregulated in T cells upon IL-4 signaling and we demonstrated that CD22 is expressed at the surface of IL-4-induced T_{VM} specifically, whereas IL-4 did not upregulate CD22 in virus-specific effector/memory T cells, thymocytes or $CD4^+$ T cells. At the cell surface of B lymphocytes, CD22 creates homo-oligomers and also binds to CD45 *in cis* via interactions with α2,6-linked sialic acids[37,56]. However, the B cell receptor (BCR) does not interact with CD22 via sialic acids and both BCR and CD22 are rather found in separate membrane domains[37]. In mouse models where CD22 cannot bind sialic acid[57], less CD22 homo-oligomers are formed, resulting in increased association with the BCR. We have not investigated to which ligand(s) T_{VM} CD22 binds, but we did observe that the $CD22^+$ T_{VM} had a distinct functional phenotype and expressed a diverse TCR repertoire enriched in features of self-reactivity when compared to naive T cells and from $CD22^-$ T_{VM} in response to IL-4. Previous reports showed that IL-4-responding antigen-specific T_{TM} had an altered effector phenotype with reduced NKG2D or CCL5 expression[58], but our results highlighted that IL-4 production in response to helminth infection drives an enrichment of genes involved in TCR signaling, cytotoxicity, cell cycle, and the STAT-5 activation pathway. TCR activation is supported by the enriched features of CDR3 sequences associated with self-reactivity, similar to that observed in regulatory T cells (Tregs)[17,22,59]. EOMES has been involved in driving self-reactive T_{VM} in the thymus[17]. Thus, it is possible that IL-4 induces an effector/memory program in self-specific T_{VM} via EOMES activation which is then counter-regulated by CD22 expression. This possibility is also supported by the observed upregulation of the proto-oncogene Src tyrosine protease *Fyn*, related to the oncogene *Lyn* which is required for CD22 inhibitory activity in B lymphocytes as well as increased expression of the adaptor protein-encoding gene *Grb2* which interacts with the immunoreceptor tyrosine-based inhibitory motif (ITIM) of CD22[60]. However, CD22 might not be the only inhibitory strategy to counter-regulate IL-4-responding T_{VM}, since increased expression of CD39, CD160, or inhibitory Ly49e/g was also observed in $CD22^+$ T_{VM}. Interestingly, $CD8^+$ T cells expressing inhibitory Ly49 or related killer cell immunoglobulin-like (KIR) receptors in mouse or human, respectively, have been reported to ensure immunoregulation and control immunopathology[61,62]. CD39 was even more strongly expressed in $Cd22^{-/-}$, suggesting the absence of CD22 might be at least partially compensated

by upregulation of alternative regulatory receptors. Indeed, although germline *Cd22*$^{-/-}$ mice had similar worm control than WT mice and responded to helminth infection by expanding similar levels of T_{VM}, naive *Cd22*$^{-/-}$ mice had higher numbers of T_{VM} in steady-state, and *Cd22*$^{-/-}$ T_{VM} in mixed-bone marrow chimeras strongly responded to IL-4 by producing significantly more GZMA, EOMES and IFN-γ. Thus, CD22 contributes as a peripheral tolerance regulator of self-reactive T_{VM} expansion in response to IL-4 during worm infection. It now remains to be determined how such IL-4-activation of self-reactive T_{VM} and induction of CD22 is a transient phenomenon or if it leaves an imprint to train CD22^{+} T_{VM} in the long term.

MATERIALS AND METHODS

Mice

The experiments, maintenance and care of mice and rats complied with the guidelines of the European Convention for the Protection of Vertebrate Animals used for Experimental and other Scientific Purposes (CETS n° 123). The protocol was approved by the Committee on the Ethics of Animal Experiments of the University of Liège, Belgium (Permit nos. 2001 and 2371). All efforts were made to minimize suffering. Female BALB/cAnNCrl and C57BL/6NCrl wild-type mice, 6–8 weeks old, were purchased from Charles River. *E8i*^{Cre} genitor mice were obtained from Prof. A. Thiel (C57BL/6-Tg(Cd8a-cre)1Itan/J*,* Charité Berlin, Germany). BALB/c CD45.1^{+} genitor mice were generously provided by Prof. U. Eriksson (Center for Molecular Cardiology, University of Zurich). CSP-TCR transgenic Thy1.1 mice were obtained from Dr R. Amino (Institut Pasteur, Paris, France). OT-I TCR transgenic *Rag*$^{-/-}$ mice were obtained from Prof. S. Goriely, Université Libre de Bruxelles, Belgium). Thy1.2.1 (Thy1.1^{+}Thy1.2^{+}) BALB/c mice were obtained by crossing Thy1.1 BALB/c with WT BALB/c. *Il4ra*$^{-/-}$ BALB/c and *Il4ra*$^{lox/lox}$ BALB/c mice were initially obtained from Prof. F. Brombacher (University of Cape Town, South Africa). CD45.1.2 (CD45.1^{+}CD45.2^{+}) C57BL/6 mice were obtained by crossing CD45.1 with CD45.2 C57BL/6 mice. *Cd22*$^{-/-}$ (C57BL/6-*Cd22*^{tm1Lam} /J) were obtained from a colony in Erlangen, Germany. Female BALB:B mice (C.B10-*H2*^{b}/LilMcdJ), that are BALB/c congenic for the C57BL/10-derived H-2^{b} region, were obtained from Dr O. Denis (Sciensano, Belgium). GREAT IFN-γ reporter mice (B6.129S4-*Ifng*$^{tm3.1Lky}$/J) have an IRES-eYFP reporter cassette inserted between the translational stop codon and 3' UTR/polyA tail of the *Ifng* gene and were obtained from Jax laboratories. WT C57BL/6 and *Stat6*$^{-/-}$ mice obtained from The Jackson Laboratory and germ-free obtained from the McGill Centre for Microbiome Research were handled with accordance with the McGill University Health Centre Research Institute Animal Resource Division with approved animal use permit no. 7977. Six- to eight-week-old female littermates were randomly assigned to experimental groups. During experiments, 4 to 5 mice were cohoused per cage, food and water was provided ad libitum. All the animals were bred and/or housed at the University of Liège, GIGA-ULiège and Department of Infectious Diseases or at the McGill University Health Centre Research Institute.

Reconstitution of germ-free mice

To colonize GF mice with specific-pathogen-free microbiota (exGF), fresh fecal pellets from C57BL/6 WT mice were homogenized in PBS to a concentration of 62.5 g mL^{-1}. The fecal slurry was centrifuged at 700 × g for 5 min to remove large debris. The supernatant was collected and diluted by ten-fold in PBS before being administered to 6-8 week old GF mice (150 µL per mouse by gavage). exGF were used 3-4 weeks after microbial reconstitution.

Parasites

The lifecycle of *H. polygyrus* was maintained in male C57BL/6 mice as described previously[63]. Briefly, 6-8-week-old male C57BL/6 mice were infected with 300 *H. polygyrus* L3 larvae in 200 µL of distilled water by oral gavage. After 14 days post infection, the mice were placed on a grid and fecal pellets collected after several hours. Then, the feces were mixed with granulated charcoal at a ratio of at least a 1:1, to achieve a consistency just damp enough with distilled water to adhere to filter paper. A thin layer was smeared on the center of dampened filter paper in a petri dish placed in a humid box in the dark. The larvae form a ring around the edge of the filter paper and were collected from day 7 onwards for at least three occasions before the paper was discarded. The larvae were collected in distilled water in a 15 mL tube and washed in cold dH_2O and centrifuged at 150 x *g* for 5 min a total of ten times. The purified *H. polygyrus* L3 larvae were stored in distilled water at 4 °C for up to 6 months. For experiments, L3 larvae were washed in distilled water 3 times before administration of 200 × L3 larvae in 200 µL distilled water by gavage. For infection of GF and exGF mice, the *H. polygyrus* lifecycle was maintained in axenic conditions as described[64]. *S. mansoni*-exposed Swiss-Webster mice were provided by the Schistosome Research Reagent Resource Center for distribution by BEI Resources, NIAID, NIH: *Schistosoma mansoni*, Strain NMRI exposed *Biomphalaria glabrata*, Strain NMRI (NR-21962), *S. mansoni*, Strain NMRI exposed Swiss-Webster mice (NR-21963). *S. mansoni* cercariae were collected from *S. mansoni* exposed *B. glabrata* and used for natural infection. *S. mansoni* eggs used for egg immunization, were collected from *S. mansoni*-exposed Swiss-Webster mouse liver and stored in PBS at −80 °C, as previously described with minor modifications[6]. Treatment with *S. mansoni* eggs consisted of an intraperitoneal immunization on day 0 (5000 eggs per mouse) followed by one intravenous injection of 5000 eggs on day 14.

Viruses

The MHV-68 strain of Murid Herpesvirus-4 (MuHV-4) expressing luciferase under the control of the M3 promoter (MuHV-4-Luc) was propagated, semi-purified and titrated in BHK-21 cells, as described[6]. Mice were infected intranasally under gas anesthesia (isoflurane) with 30 µL sterile PBS containing 10^4 PFU.

IL-4 complex treatment

Mice received 2 intraperitoneal injections of IL-4c: 5 µg of recombinant IL-4 (BioLegend, carrier-free) and 25 µg of anti-IL-4 antibody (BioLegend, clone 11B11, LEAF purified) per mouse at d0 and d2.

Cell preparation.

Spleen, thymus and lymph nodes were harvested, cut in small pieces using scissors and filtered through a 100 µm cell strainer with a sterile syringe plunger. Erythrocytes were lysed in red cell lysis solution (155 mM NH_4Cl, 0.12 mM EDTA, 10 mM $KHCO_3$), and leukocytes suspended in PBS and filtered through a 40 µm cell strainer before being counted in a Neubauer cytometer chamber with 0.4% buffered trypan blue dye for exclusion of dead cells.

Antibodies and flow cytometry.

Incubations were performed in FACS buffer (PBS containing 0.1% BSA and 0.05% NaN3) at 4°C. Cells were first incubated with anti-mouse CD16/32 antibody (clone 93, 1 µg mL^{-1}, isotype Rat IgG2a, λ, BioLegend) before fluorochrome-conjugated antibodies against surface antigens were added and incubated during 20 min at 4 °C. Various panels were used including antibodies to CD3ε (145-2C11, 0.4 µg mL^{-1}, APC-Cy7, Armenian Hamster IgG1, κ), CD183 (CXCR3-173, 2 µg mL^{-1}, BV421 or PE, Armenian Hamster IgG1, κ), CD49d (R1-2, 1 µg mL^{-1}, BV650 or BV786, CDF IgG2b, κ), CD124 (mIL4R-M1, 1 µg mL^{-1}, PE or BV421, Lewis IgG2a, κ), CD195 (C34-3448, 2 µg mL^{-1}, BV711, Rat IgG2c, κ), CD62L (MEL-14, 1 µg mL^{-1}, FITC, CDF IgG2a, κ), CD4 (GK1.5, 2 µg mL^{-1}, BUV395, Rat IgG2b, κ), CD44 (IM7, 0.4 µg mL^{-1}, BV786, Rat IgG2b, κ) all from BD Biosciences, antibody to CD3e (145-2C11 or 17A2, 0.4 µg mL^{-1}, V450 or APC, Armenian Hamster IgG or Rat IgG2b, κ), TCRβ chain (H57-597, 0.8 µg mL^{-1}, BV711, Armenian Hamster IgG), CD8α (53-6.7, 1 µg mL^{-1}, FITC or APC or BV785 or APC/Fire 750, Rat IgG2a, κ; 2 µg mL^{-1}, BV605, Rat IgGa, κ), CD44 (IM7, 0.4 µg mL^{-1}, PE-Cy7, Rat IgG2b, κ), CD183 (CXCR3-173, 2 µg mL^{-1}, FITC or APC, Armenian Hamster IgG), CD124 (I015F8, 1 µg mL^{-1}, APC, Lewis IgG2a, κ), CD39 (Duha59, 2 µg mL^{-1}, APC or PE-Cy7, Rat IgG2a, κ), CD4 (GK1.5 or RM4-5, 0,4 µg mL^{-1}, FITC or APC, Rat IgG2b, κ), CD24 (M1/69, 2 µg mL^{-1}, APC/Fire 750, Rat IgG2b, κ), CD45.1 (A20, 2 µg mL^{-1}, APC-Cy7 or APC or Alexa Fluor 700, Mouse (A.SW) IgG2a, κ), CD45.2 (104, 1 µg mL^{-1}, BV510 or PE-Cy7 or Alexa Fluor 700, Mouse (SJL) IgG2a, κ), CD90.1 (OX-7, 2,5 µg mL^{-1}, APC or Alexa Fluor 700, Mouse IgG1, κ), CD90.2 (53-2.1, 1 µg mL^{-1}, BV421, Rat IgG2a, κ), CD192 (SA203G11, 2 µg mL^{-1}, BV650, Rat IgG2b, κ), CD160 (7H1, 2 µg mL^{-1}, PerCP-Cy5.5, Rat IgG2a, κ), TCR Vβ8.1, 8.2 (MR5-2, 2 µg mL^{-1}, PE, Mouse IgG2a, κ) from BioLegend, CD45.2 (104, 2 µg mL^{-1}, eFluor450, Mouse IgG2a, κ), TCRβ chain (H57-597, 2 µg mL^{-1}, APC-eF780, Armenian Hamster IgG), CD49d (R1-2, 2 µg mL^{-1}, PerCP710 or PE, Rat IgG2b, κ), CD4 (RM4-5, 2 µg mL^{-1}, AF700, Rat IgG2a, κ), CD44 (IM7, 2 µg mL^{-1}, PE, Rat IgG2b, κ) from ThermoFisher and antibodies to CD22 (Cy34.1, 3 µg ml^{-1}, PE or biotinylated, isotype mouse IgG1κ) from Miltenyi Biotec. Biotinylated antibodies were detected using Qdot 625-conjugated streptavidin (5 nM, ThermoFisher). Dead cells were stained using Zombie Aqua Fixable Viability Kit (1000x dilution, Biolegend) or Fixable Viability Dye (1000× dilution, eFluor780 or eFluor 506,

559 eBioscience). For detection of intracellular IFN-γ (XMG1.2, BV711 (2 µg mL^{-1}, Biolegend) or
560 PE (2 µg mL^{-1}, Biolegend), or AF488 (5 µg mL^{-1}, ThermoFisher) or APC (2 µg mL^{-1},
561 ThermoFisher), Rat IgG1, κ), GATA3 (TWAJ, 5 µL per test, PerCP710, Rat IgG2b, κ,
562 ThermoFisher) and GZMA (3G8.5, 2 µg mL^{-1}, PE (BioLegend) or APC (ThermoFisher), Mouse
563 IgG2b, κ), cells were fixed in paraformaldehyde 2% in PBS on ice for 20 min, before
564 permeabilized and stained in FACS buffer containing 0.1% saponin for 30 min at 4°C. In
565 experiments in which intranuclear staining for transcription factors was needed, cells were
566 fixed and permeabilized using Foxp3/Transcription factor staining buffer set (eBioscience)
567 following manufacturer's instruction and incubated 30 min at 4°C with antibody against EOMES
568 (Dan11mag, 2 µg mL^{-1}, PE or PE-eFluor610, Rat IgG2a, κ, eBioscience, or X4-83, 2 µg mL^{-1},
569 Alexa Fluor 488, Mouse IgG1, κ, BD Biosciences) diluted in permeabilization buffer. Samples
570 were analyzed on a BD Fortessa X-20 flow cytometer (BD Biosciences). Flow cytometry
571 acquisitions were analyzed using FlowJo 10.8. In some analyses, samples were concatenated
572 and further analyzed using the built-in plugins UMAP and FlowSOM. In some experiments,
573 samples were analyzed using an ImageStream X Mk II (Amnis, VIB Flow Core Facility,
574 UGhent). For tetramer stainings, cells were incubated with BV421-conjugated tetramers H-
575 $2D^b$-$ORF6^{487-495}$ (AGPHNDMEI, 90 nM) or H-$2K^b$-$ORF61^{521-531}$ (TSINFVKI, 45 nM) (NIH
576 Tetramer Core Facility) for 30min at RT before further staining.
577
578 ***Ex vivo* restimulation and cytokine production**
579 Cytokine production upon restimulation was assessed by intracellular cytokine staining (ICCS)
580 and flow cytometry. For ICCS, cells were cultured at 37°C, 5% CO_2 in IMDM complemented
581 with 2 mM β-mercaptoethanol, 100 U mL^{-1} penicillin, 100 mg mL^{-1} streptomycin and 10% fetal
582 calf serum for 4h in presence of brefeldin A (10 µg mL^{-1}, Sigma-Adlrich), monensin (2 µM,
583 eBioscience). Unbiased restimulation was performed using phorbol 12-myristate 13-acetate
584 (PMA, 20 ng mL^{-1}, Sigma-Adlrich) and ionomycin (1 µg mL^{-1}, Sigma-Aldrich). Innate
585 restimulation was performed using IL-12 (5 ng mL^{-1}, BioLegend) and IL-18 (10 ng mL^{-1},
586 BioLegend) for 16h and brefeldin A was added for the last 3h of incubation. TCR-specific
587 restimulation was done using anti-CD3 (145-2C11, 1 µg mL^{-1}, purified, BioLegend) and anti-
588 CD28 (37.51, 1 µg mL^{-1}, purified, BioLegend) mixed with brefeldin A and monensin for 4h.
589 Following surface and viability stainings, cells were fixed in 2% paraformaldehyde overnight
590 and washed with Permeabilization Buffer (eBioscience) before being incubated with antibodies
591 against IFN-γ (clone XMG1.2, 2 µg mL^{-1}, BV711 or PE, Rat IgG1, κ, BioLegend) in
592 Permeabilization Buffer for 20 min at 4°C.
593
594
595

Cell isolation for single-cell RNA-seq assay

Single-cell suspension were obtained from harvested spleen or mesLN before enrichment of $CD8^+$ T lymphocytes using the MojoSort Mouse CD8 T Cell Isolation Kit (Biolegend) and LS columns (Miltenyi Biotec). For spleen samples, enriched $CD8^+$ T cells isolated from mice of the same genotype and having received the same treatment were individually stained with 0.5 µg per 1.5 million cells of TotalSeq anti-mouse hashtag antibodies (A0301 to A0305, Biolegend) and incubated at 4°C during 20 min before pooling (n=4 to 5). Pools were then filtered through a 40 µm cell strainer and the concentration adjusted to 700 to 1000 cells μL^{-1} before single cell capture using the Chromium controller (10x Genomics). For mesLN samples, enriched $CD8^+$ T cells from IL-4RαΔ^{CD8} mice were pooled and further sorted to high purity based on the expression of CD124. Then, $CD124^+$ or $CD124^-$ were stained with 20 µL per 1 million cells of Sample Tag 1 or Sample Tag 2 from the Mouse Immune Single-Cell Multiplexing Kit (BD Biosiences) and pooled before filtered through a 40 µm cell strainer, before being subjected to single cell capture and quality control using the BD Rhapsody Express and BD Rhapsody Scanner (BD Biosiences).

Mixed bone-marrow chimeric mice models.

Mixed bone-marrow chimeric mice were produced by treating $Thy1.1^+Thy1.2^+$ BALB/c mice (Thy1.2.1) or $CD45.1^+CD45.2^+$ C57BL/6 mice (CD45.1.2) with intraperitoneal injection of busulfan (25 µg g^{-1} of mouse body weight per day for 3 consecutive days, Cayman Chemical) for myeloablation, as previously reported[72]. Then, mice were reconstituted by intravenous injection of 2×10^6 bone marrow cells 24h after the last busulfan injection. Bone marrow cells were obtained from femurs and tibias of donor $CD45.1^+$ WT and $CD45.2^+$ *Il4ra*$^{-/-}$ mice, or of donor $CD45.1^+$ WT and $CD45.2^+$ *Cd22*$^{-/-}$ mice and mixed at a 1:1 ratio before intravenous injection in 100 µL sterile PBS into Thy1.2.1 mice or CD45.1.2 mice, respectively. Mice were left untreated for 6 weeks to allow complete reconstitution and chimerism of circulating $CD8^+$ T cells was then confirmed by flow cytometry, before used in experiments.

Single-cell RNA library preparation

Spleen samples were processed using the 10x genomics Chromium Single Cell 3' v3 chemistry as per the manufacturer's recommendations (10x Genomics). Samples obtained from mesLN were processed using the BD Rhapsody Whole Transcriptome Analysis cDNA synthesis and amplification kit as per the manufacturer's recommendations (BD Biosiences). Barcoded RNA was collected and processed following the manufacturer's recommendations. After quantification, equal molar concentration of each library was pooled and sequenced using the NovaSeq S4 300 cycles XP workflow (GIGA ULiege, Belgium).

Single-cell RNA-seq analysis

Raw data processing. For 10x Genomics platform, the sequencing run was processed using Cell Ranger (v3.0.2). For BD Rhapsody platform, sequencing run was processed using SevenBridges Genomics. First using mkfastq function to produce fastq files and then the count function to perform alignment, filtering, barcode counting, and UMI counting. The merged data were transferred to the R statistical environment for analysis using the package Seurat (v3.1.5)[65]. *Doublet cell filtering.* Cell Hashing/HTO libraries were processed using CITE-seq Count python package v1.4.3 (https://github.com/Hoohm/CITE-seq-Count) and used in Seurat to remove identified Doublet cells. Sample Tag demultiplexing for BD Rhapsody platform was performed using the build-in function in SevenBridges Genomics. *Data cleaning.* We additionally applied two filtering steps as we selected cells with a total number of molecules detected within a range between 2000 and 10,000 and a percentage of reads that map to the mitochondrial genome lower than 10%. *Samples integration & Transcriptome-based clustering.* We used Seurat SCTransform workflow for Multiple Dataset Integration in order to merge all the datasets and proceed with joint analysis. We used FindIntegrationAnchors and IntegrateData functions based on SCT normalization. We then performed PC analysis with RunPCA algorithm producing 50 PCs and we applied FindNeighbors and FindClusters functions from Seurat with two chosen parameters (dims = 1:50; resolution = 0.5) to identify clusters. *Data visualization.* Data were then dimensionally reduced for visualization using RunUMAP function and using (dims = 1:50). UMAP figures were obtained using DimPlot function with UMAP reduction. Other plot types were generated using implemented Seurat functions, custom R scripts or combinations of both. *SingleR for cluster annotation and selection.* SingleR package was performed for unbiased annotation and was performed against the build-in ImmGen database in SingleR package. Clusters showing expression of CD8a and CD3e were selected, and other clusters were removed. Cells presenting T8.memory or T8.effector profiles were selected for additional analysis. New clustering of this subset of cells was performed using same methodology as previously described. *Single-cell differential gene expression analysis.* Cluster specific markers were obtained by the FindAllMarkers function of Seurat with default parameters. Pairwise single-cell differential gene expression analysis was performed between condition inside clusters using the FindMarkers function with default parameters. *Gene set enrichment analysis*. TF-gene interactions were extracted from mouse DoRothEA database[66], while filtering for high-confidence interactions (score A, B, or C). TF activities were then inferred from differential gene expression results using fgsea[67], with signed logarithm of p-value used as the metric to rank the genes. Method details are available here https://github.com/BlanQwall/VM_T (*credentials : ID: FictiveReviewer - Password: ImmunoPhysiology*).

RNA sequencing.

Single-cell suspension were obtained from harvested spleens before enrichment of $CD8^+$ T lymphocytes using the MojoSort Mouse CD8 T Cell Isolation Kit (Biolegend) and LS columns (Miltenyi Biotec). Then, around 100,000 cells were sorted in IMDM 50% FCS using a FACS Aria IIIu (BD biosciences). Total RNA was purified using the RNAeasy Micro Kit (Qiagen) and eluted in 14µL of water. RNA integrity was further verified using a 2100 Agilent Bioanalyzer and RIN > 9 were used for further analyses. Total RNA was then used as input for the SMART-seq HT cDNA synthesis kit (Takara). Libraries were quality checked on an Agilent Bioanalyzer, pooled at an equimolar ratio and sequenced on a Novaseq S4 V1.5 with 300 cycles XP workfow. Reads were mapped to the mouse reference genome (mm10) using STAR (version 3.4.0). Subsequently the analysis was performed with R Bioconductor packages Rsamtools (version 1.18.3) and GenomicAlignments (version 1.2.2) were used to count the reads by exons, and gene count datasets were then analyzed to determine DE genes (DEGs) using DESeq2 (version 1.16.1). A gene was determined to be a DEG by passing FDR < 0.01 and log 2-fold change ≥ ±1.

TCR sequencing

Single-cell suspensions were obtained from harvested spleens before enrichment of $CD8^+$ T lymphocytes using the MojoSort Mouse CD8 T Cell Isolation Kit (Biolegend) and LS columns (Miltenyi Biotec). Then, 200,000 cells were sorted in IMDM 50% FCS using a FACS Aria IIIu (BD biosciences). RNA extraction was carried out using the RNeasy Micro Kit (Qiagen, 217084). High-throughput sequencing was performed as previously described with template-switch anchored RT-PCR[68] but using oligodT during the cDNA generation and the following mouse-specific Cα and Cβ primers for the PCR amplification: TRAC '5-*GTCTCGTGGGCTCGGAGATGTGTATAAGAGACAG*GTCCTGAGACCGAGGATCTTT and TRBC '5-*GTCTCGTGGGCTCGGAGATGTGTATAAGAGACAG*GGGTAGCCTTTTGTTTGT-TTG (adapters in italic).

CDR3 sequence analysis

CDR3 sequences were extracted from raw sequencing fastq files after aligning the reads to reference V, D and J genes from 'TRA' or 'TRB' loci of GenBank database using the MiXCR software (version 3.0.12)[69]. CDR3 sequences were further analyzed using VDJtools software version 1.2.1[70]. CDR3 extraction was also performed on raw fastq files derived from RNA-seq experiments to increase the robustness of the data in all analyzed groups, this analysis was performed following the standard pipeline for CDR3 extraction from RNA-seq data described in MiXCR documentation. In all cases out of frame sequences were excluded from the analysis, as well as non-functional TRA and TRB segments using IMGT (the international

ImMunoGeneTics information system®) annotation. Cumulative gene segment plots were generated using the output from CalcSegmentUsage function. Tree maps were generated using the Treemap Package (version 2.4.3) on RStudio. Diversity read-outs (Normalized Shannon-Wiener, Inverse Simpson, Chao1 and efronThisted indexes) were obtained from the re-sampled file generated using CalcDiversityStats function. Cysteine usage was determined following previously described indications[71]. Hydrophobic doublets in CDR3α and CDR3β sequences were determined by calculating the percentage of sequences using any of the 175 amino acid doublets previously identified as promoters of self-reactivity[45]. Physicochemical properties were computed on the 5 central amino acids from the CDR3 sequences using CalcCdrAaStats function from VDJtools software. Principal component analysis of CDR3α and CDR3β repertoire was performed using R package FactoMineR (version 2.7) and using the variables described in **Extended Data Fig. 8i** which were scaled to similar range using Z-score normalization prior to PCA analysis. PCA results were visualized using factoextra (version 1.0.7) R package.

Statistical analysis

Statistical evaluation of different groups was performed either by analysis of variance (ANOVA) followed by the Dunnett or Sidak multiple-comparison test or by non-parametric Mann-Whitney test, as indicated. A p-value < 0.05 was considered significant. Statistical analyses were performed using Prism v8 and v9 (GraphPad, La Jolla, CA).

ACKNOWLEDGEMENTS

The authors are thankful to S. Li for his help in GSEA analyses, L. Gillet for insightful discussions, and the technician and administrative team of the Immunology-Vaccinology laboratory, and L. Karim and members of the GIGA Genomics platform. We also thank C. Faubert at the MI4 Gnotobiotic Animal Research Platform for her expertise and assistance with the germ-free helminth infections. The following tetramers were obtained through the NIH Tetramer Facility: H-2D^{b}-ORF6$^{487-495}$, H-2K^{b}-ORF61$^{524-531}$. *B. glabrata* snails were provided by Dr J. Vicogne, Institut Pasteur Lille, France.

Funding

B.Y. is supported by the Chinese Scholarship Council. G.S.S. is supported by Télévie-FNRS (7.4586.19 and 922 7.6529.21). A.M.A. is supported by a doctoral training award from FRQS. D.V. FNRS CDR (CDR_J.0225.20) and WELBIO (WELBIO-CR-2022 A – 15). B.G.D. FNRS CDR (CDR/OL J.0062.20) and ULiège (FSR-S-SS-19/43 and ARC 19-23/11). This work was supported by the Canadian Institutes of Health Research (PJT-362757). H.S.N. holds a Canada Research Chair in Systems Biology of Gene Regulation. I.L.K. holds a Canada Research Chair in Barrier Immunity. B.G.D. is a Senior Research Associate of the Fonds de la Recherche Scientifique (F.R.S.-FNRS).

Author Contributions

B.Y. designed and performed the experiments, analyzed the data, and wrote the paper. G.S.S. performed TCR sequencing, CDR3 analyses and contributed to the manuscript preparation. O.P., G.P., G.P. and B.K. performed the experiments and analyzed the data. G.V.I. and J.V.D. performed the ImageStream analyses. A.L., A.M.A. and Q.B. provided support for the analysis of RNA sequencing data. B.M. supervised mouse breeding and provided the GREAT mice and contributed to manuscript preparation. T.M. contributed to manuscript preparation. D.V., H.S.N., I.K. contributed the design of experiments and to the manuscript preparation. L.N. supervised mouse breeding and provided the CD22 knockout mice and contributed to manuscript preparation. B.G.D. planned and supervised the work, acquired funding, designed experiments, prepared the figures and wrote the paper.

Competing interests

The authors declare no competing interests.

REFERENCES

1. Pullan, R. L., Smith, J. L., Jasrasaria, R. & Brooker, S. J. Global numbers of infection and disease burden of soil transmitted helminth infections in 2010. *Parasit Vectors* **7**, 37 (2014).
2. Hotez, P. J. *et al.* Helminth infections: the great neglected tropical diseases. *J Clin Invest* **118**, 1311–1321 (2008).
3. Jourdan, P. M., Lamberton, P. H. L., Fenwick, A. & Addiss, D. G. Soil-transmitted helminth infections. *The Lancet* **391**, 252–265 (2018).
4. Harris, N. L. & Loke, P. Recent Advances in Type-2-Cell-Mediated Immunity: Insights from Helminth Infectionfile:///Applications/Mendeley%20Reference%20Manager.app/Contents/Resources/app.asar/dist/production.html#/library. *Immunity* **47**, 1024–1036 (2017).
5. Vacca, F. & le Gros, G. Tissue-specific immunity in helminth infections. *Mucosal Immunology 2022 15:6* **15**, 1212–1223 (2022).
6. Rolot, M. *et al.* Helminth-induced IL-4 expands bystander memory CD8+ T cells for early control of viral infection. *Nat Commun* **9**, 4516 (2018).
7. Lin, J. S. *et al.* Virtual memory CD8 T cells expanded by helminth infection confer broad protection against bacterial infection. *Mucosal Immunol* (2018) doi:10.1038/s41385-018-0100-x.
8. Tripathi, P. *et al.* IL-4 and IL-15 promotion of virtual memory CD8+ T cells is determined by genetic background. *Eur J Immunol* **46**, 2333–2339 (2016).
9. Hussain, T. *et al.* Helminth Infection–Induced Increase in Virtual Memory CD8 T Cells Is Transient, Driven by IL-15, and Absent in Aged Mice. *The Journal of Immunology* **210**, 297–309 (2023).
10. Laidlaw, B. J., Craft, J. E. & Kaech, S. M. The multifaceted role of CD4(+) T cells in CD8(+) T cell memory. *Nat Rev Immunol* **16**, 102–111 (2016).
11. Seo, I. H. *et al.* IL-15 enhances CCR5-mediated migration of memory CD8+ T cells by upregulating CCR5 expression in the absence of TCR stimulation. *Cell Rep* **36**, 109438 (2021).
12. Lee, J. Y., Hamilton, S. E., Akue, A. D., Hogquist, K. A. & Jameson, S. C. Virtual memory CD8 T cells display unique functional properties. *Proc Natl Acad Sci U S A* **110**, 13498–13503 (2013).
13. Haluszczak, C. *et al.* The antigen-specific CD8+ T cell repertoire in unimmunized mice includes memory phenotype cells bearing markers of homeostatic expansion. *J Exp Med* **206**, 435–448 (2009).
14. Hou, S. *et al.* Virtual memory T cells orchestrate extralymphoid responses conducive to resident memory. *Sci Immunol* **6**, (2021).
15. Jameson, S. C. & Masopust, D. Understanding Subset Diversity in T Cell Memory. *Immunity* **48**, 214–226 (2018).
16. White, J. T., Cross, E. W. & Kedl, R. M. Antigen-inexperienced memory CD8+ T cells: where they come from and why we need them. *Nat Rev Immunol* **17**, 391–400 (2017).
17. Miller, C. H. *et al.* Eomes identifies thymic precursors of self-specific memory-phenotype CD8+ T cells. *Nat Immunol* 1–11 (2020) doi:10.1038/s41590-020-0653-1.
18. Martinet, V. *et al.* Type I interferons regulate eomesodermin expression and the development of unconventional memory CD8(+) T cells. *Nat Commun* **6**, 7089 (2015).
19. Hussain, T. & Quinn, K. M. Similar but different: virtual memory CD8 T cells as a memory-like cell population. *Immunology and Cell Biology* vol. 97 675–684 Preprint at https://doi.org/10.1111/imcb.12277 (2019).
20. Quinn, K. M. *et al.* Age-Related Decline in Primary CD8(+) T Cell Responses Is Associated with the Development of Senescence in Virtual Memory CD8(+) T Cells. *Cell Rep* **23**, 3512–3524 (2018).
21. White, J. T. *et al.* Virtual memory T cells develop and mediate bystander protective immunity in an IL-15-dependent manner. *Nat Commun* **7**, 11291 (2016).

22. Drobek, A. *et al.* Strong homeostatic TCR signals induce formation of self-tolerant virtual memory CD8 T cells. *EMBO J* **37**, (2018).
23. Weinreich, M. A. *et al.* KLF2 transcription-factor deficiency in T cells results in unrestrained cytokine production and upregulation of bystander chemokine receptors. *Immunity* **31**, 122–130 (2009).
24. Weinreich, M. A., Odumade, O. A., Jameson, S. C. & Hogquist, K. A. T cells expressing the transcription factor PLZF regulate the development of memory-like CD8+ T cells. *Nat Immunol* **11**, 709–716 (2010).
25. Renkema, K. R. *et al.* IL-4 sensitivity shapes the peripheral CD8+ T cell pool and response to infection. *J Exp Med* **213**, 1319–1329 (2016).
26. Sosinowski, T. *et al.* CD8alpha+ dendritic cell trans presentation of IL-15 to naive CD8+ T cells produces antigen-inexperienced T cells in the periphery with memory phenotype and function. *J Immunol* **190**, 1936–1947 (2013).
27. Lee, Y. J., Holzapfel, K. L., Zhu, J., Jameson, S. C. & Hogquist, K. A. Steady-state production of IL-4 modulates immunity in mouse strains and is determined by lineage diversity of iNKT cells. *Nat Immunol* **14**, 1146–1154 (2013).
28. Lauvau, G. & Goriely, S. Memory CD8+ T Cells: Orchestrators and Key Players of Innate Immunity? *PLoS Pathog* **12**, e1005722 (2016).
29. Shimokawa, C. *et al.* CD8+ regulatory T cells are critical in prevention of autoimmune-mediated diabetes. *Nat Commun* **11**, 1922 (2020).
30. Rifa'i, M., Kawamoto, Y., Nakashima, I. & Suzuki, H. Essential roles of CD8+CD122+ regulatory T cells in the maintenance of T cell homeostasis. *J Exp Med* **200**, 1123–1134 (2004).
31. Maekawa, Y. *et al.* Notch2 integrates signaling by the transcription factors RBP-J and CREB1 to promote T cell cytotoxicity. *Nat Immunol* **9**, 1140–7 (2008).
32. Wada, H. *et al.* Requirement for intron structures in activating the Cd8a locus. *Proc Natl Acad Sci U S A* **115**, 3440–3445 (2018).
33. Aran, D. *et al.* Reference-based analysis of lung single-cell sequencing reveals a transitional profibrotic macrophage. *Nature Immunology 2019 20:2* **20**, 163–172 (2019).
34. la Manno, G. *et al.* RNA velocity of single cells. *Nature 2018 560:7719* **560**, 494–498 (2018).
35. White, J. T. *et al.* Virtual memory T cells develop and mediate bystander protective immunity in an IL-15-dependent manner. *Nat Commun* **7**, 11291 (2016).
36. Müller, J. & Nitschke, L. The role of CD22 and Siglec-G in B-cell tolerance and autoimmune disease. *Nature Reviews Rheumatology 2014 10:7* **10**, 422–428 (2014).
37. Meyer, S. J., Linder, A. T., Brandl, C. & Nitschke, L. B Cell Siglecs–News on Signaling and Its Interplay With Ligand Binding. *Front Immunol* **9**, (2018).
38. Pluvinage, J. v. *et al.* CD22 blockade restores homeostatic microglial phagocytosis in ageing brains. *Nature* **568**, 187–192 (2019).
39. Sathish, J. G. *et al.* CD22 is a functional ligand for SH2 domain-containing protein-tyrosine phosphatase-1 in primary T cells. *Journal of Biological Chemistry* **279**, 47783–47791 (2004).
40. Hudson, W. H. *et al.* Proliferating Transitory T Cells with an Effector-like Transcriptional Signature Emerge from PD-1+ Stem-like CD8+ T Cells during Chronic Infection. *Immunity* **51**, 1043-1058.e4 (2019).
41. Miller, C. H. *et al.* Eomes identifies thymic precursors of self-specific memory-phenotype CD8+ T cells. *Nat Immunol* 1–11 (2020) doi:10.1038/s41590-020-0653-1.
42. Drobek, A. *et al.* Strong homeostatic TCR signals induce formation of self-tolerant virtual memory CD8 T cells. *EMBO J* **37**, (2018).
43. Tarakhovsky, A. *et al.* A Role for CD5 in TCR-Mediated Signal Transduction and Thymocyte Selection. *Science (1979)* **269**, 535–537 (1995).
44. Azzam, H. S. *et al.* CD5 Expression Is Developmentally Regulated By T Cell Receptor (TCR) Signals and TCR Avidity. *Journal of Experimental Medicine* **188**, 2301–2311 (1998).

45. Stadinski, B. D. *et al.* Hydrophobic CDR3 residues promote the development of self-reactive T cells. *Nature Immunology 2016 17:8* **17**, 946–955 (2016).
46. Daley, S. R. *et al.* Cysteine and hydrophobic residues in CDR3 serve as distinct T-cell self-reactivity indices. *Journal of Allergy and Clinical Immunology* **144**, 333–336 (2019).
47. Logunova, N. N. *et al.* MHC-II alleles shape the CDR3 repertoires of conventional and regulatory naïve CD4+ T cells. *Proc Natl Acad Sci U S A* **117**, 13659–13669 (2020).
48. Hogan, T. *et al.* Clonally diverse T cell homeostasis is maintained by a common program of cell-cycle control. *J Immunol* **190**, 3985–3993 (2013).
49. Ge, Q., Bai, A., Jones, B., Eisen, H. N. & Chen, J. Competition for self-peptide-MHC complexes and cytokines between naïve and memory CD8+ T cells expressing the same or different T cell receptors. *Proc Natl Acad Sci U S A* **101**, 3041–3046 (2004).
50. Sano, G. *et al.* Swift development of protective effector functions in naive CD8(+) T cells against malaria liver stages. *J Exp Med* **194**, 173–180 (2001).
51. Nitschke, L., Carsetti, R., Ocker, B., Köhler, G. & Lamers, M. C. CD22 is a negative regulator of B-cell receptor signalling. *Current Biology* **7**, 133–143 (1997).
52. Jameson, S. C., Lee, Y. J. & Hogquist, K. A. Innate memory T cells. *Adv Immunol* **126**, 173–213 (2015).
53. Galletti, G. *et al.* Two subsets of stem-like CD8+ memory T cell progenitors with distinct fate commitments in humans Giovanni. *Nat Immunol* doi:10.1038/s41590-020-0791-5.
54. Sekine, T. *et al. TOX is expressed by exhausted and polyfunctional human effector memory CD8 + T cells*. *Sci. Immunol* vol. 5 (2020).
55. Wen, T. *et al.* The Pan-B Cell Marker CD22 Is Expressed on Gastrointestinal Eosinophils and Negatively Regulates Tissue Eosinophilia. *The Journal of Immunology* **188**, 1075–1082 (2012).
56. Akatsu, C. *et al.* The inhibitory coreceptor CD22 restores B cell signaling by developmentally regulating Cd45−/− immunodeficient B cells. *Sci Signal* **15**, (2022).
57. Muller, J. *et al.* CD22 ligand-binding and signaling domains reciprocally regulate B-cell Ca2+ signaling. *Proc Natl Acad Sci U S A* **110**, 12402–12407 (2013).
58. Ventre, E. *et al.* Negative regulation of NKG2D expression by IL-4 in memory CD8 T cells. *J Immunol* **189**, 3480–3489 (2012).
59. Logunova, N. N. *et al.* MHC-II alleles shape the CDR3 repertoires of conventional and regulatory naïve CD4+ T cells. *Proc Natl Acad Sci U S A* **117**, 13659–13669 (2020).
60. Smith, K. G. C., Tarlinton, D. M., Doody, G. M., Hibbs, M. L. & Fearon, D. T. Inhibition of the B cell by CD22: a requirement for Lyn. *J Exp Med* **187**, 807–811 (1998).
61. Li, J. *et al.* KIR+CD8+ T cells suppress pathogenic T cells and ar active in autoimmune diseases and COVID-19. *Science (1979)* **376**, (2022).
62. Kim, H. J. *et al.* CD8+ T regulatory cells express the Ly49 Class I MHC receptor and are defective in autoimmune prone B6-Yaa mice. *Proc Natl Acad Sci U S A* **108**, 2010–2015 (2011).
63. Bouchery, T. *et al.* The Study of Host Immune Responses Elicited by the Model Murine Hookworms *Nippostrongylus brasiliensis* and *Heligmosomoides polygyrus*. *Curr Protoc Mouse Biol* **7**, 236–286 (2017).
64. Russell, G. A. *et al.* A protocol for generating germ-free Heligmosomoides polygyrus bakeri larvae for gnotobiotic helminth infection studies. *STAR Protoc* **2**, 100946 (2021).
65. Stuart, T. *et al.* Comprehensive Integration of Single-Cell Data. *Cell* **177**, (2019).
66. Garcia-Alonso, L., Holland, C. H., Ibrahim, M. M., Turei, D. & Saez-Rodriguez, J. Benchmark and integration of resources for the estimation of human transcription factor activities. *Genome Res* **29**, 1363–1375 (2019).
67. Korotkevich, G. *et al.* Fast gene set enrichment analysis. *bioRxiv* 060012 (2021) doi:10.1101/060012.
68. Papadopoulou, M. *et al.* TCR Sequencing Reveals the Distinct Development of Fetal and Adult Human Vγ9Vδ2 T Cells. *J Immunol* **203**, 1468–1479 (2019).

69. Bolotin, D. A. *et al.* MiXCR: software for comprehensive adaptive immunity profiling. *Nat Methods* **12**, 380–381 (2015).
70. Shugay, M. *et al.* VDJtools: Unifying Post-analysis of T Cell Receptor Repertoires. *PLoS Comput Biol* **11**, (2015).
71. Wirasinha, R. C. *et al.* αβ T-cell receptors with a central CDR3 cysteine are enriched in CD8αα intraepithelial lymphocytes and their thymic precursors. *Immunol Cell Biol* **96**, 553–561 (2018).
72. Montecino-Rodriguez, E. & Dorshkind, K. Use of Busulfan to Condition Mice for Bone Marrow Transplantation. *STAR Protoc* **1**, 100159 (2020).

FIGURE LEGENDS

Figure 1. Impaired peripheral T_{VM} expansion in IL-4Rα$^{\Delta CD8}$ mice during helminth infection.

(**a**) Representative pseudocolour flow plot of TCRβ$^+$ thymocytes. Median fluorescence intensities (MFI) of CD124 in single positive CD8$^+$ (SP8) and CD4$^+$ thymocytes (SP4).

(**b**) Representative contour flow plot of SP8 thymocytes and representative histogram of CD24$^-$ SP8 thymocytes. Summary data of CD124$^-$ cell percentages in CD24$^-$ SP8 are shown, as determined by flow cytometry.

(**c**) Representative pseudocolour flow plot of spleen live lymphocytes and representative histogram of CD3$^+$CD8$^+$ T splenocytes. Median fluorescence intensities (MFI) of CD124 of the indicated population.

(**d**) Summary data of CD8$^+$CD3$^+$ T cell numbers and CD44^{hi}CXCR3$^+$ CD49d^{low} CD8$^+$ T cell numbers and percentages, as determined by flow cytometry.

(**e**) Representative pseudocolour flow plot of splenic CD8$^+$ T lymphocytes. Numbers indicate percent of events in each gate.

(**f**) Representative contour flow plot of splenic CD8$^+$ T lymphocytes and summary data of CD49d^{low}CXCR3$^+$ T_{VM} percentages in CD124$^+$ and CD124$^-$ CD8$^+$ T cells, as gated by flow cytometry.

(**g**-**h**) IL-4c was injected to IL-4Rα^{WT} or IL-4Rα$^{\Delta CD8}$ mice at d0 and d2 before analysis at d4. Data show summary plots of cell numbers, percentages, and median fluorescence intensities (MFI) of EOMES of the indicated populations in the thymus (**g**) or the spleen (**h**).

(**i**) Summary plots of CD124$^+$ and CD124$^-$ CD8$^+$ T cells percentages in naive or IL-4c-treated IL-4Rα$^{\Delta CD8}$ mice.

(**j**) Summary data of CD49d^{low}CXCR3$^+$ T_{VM} percentages in the spleen of IL-4Rα^{WT} or IL-4Rα$^{\Delta CD8}$ mice after treatment with IL-4c, at day 15 after *H. polygyrus* infection, and at d22 after administration of *S. mansoni* (Sm) eggs.

(**k**) Summary data of CD49d^{low}CXCR3$^+$ T_{VM} percentages in CD124$^+$ and CD124$^-$ CD8$^+$ T cells in IL-4Rα$^{\Delta CD8}$ mice, based on the results in (j).

(**l**) *H. polygyrus* adult worm burden in the gut at day 15 after infection in the indicated mouse group.

Statistical significance calculated using Mann-Whitney test (**a-f, l**) or two-way analysis of variance (ANOVA) and Sidak's multiple comparison-test (**g-k**) (*P < 0.05, *P < 0.01, ***P < 0.001, ****P < 0.0001; $^{\#\#}P$ < 0.01, $^{\#\#\#\#}P$ < 0.0001, compared with PBS-treated WT control). Data are representative of three independent experiments with 3-5 mice per group. Mean ± s.e.m., each symbol represents one individual mouse.

Figure 2. Single-cell RNA sequencing reveals T_{VM} cluster.

(**a**) UMAP visualization of unsupervised Seurat clustering analysis of combined 33,553 single $CD8^+$ T cell transcriptomes of IL-4Rα^{WT} or IL-4Rα$^{\Delta CD8}$ mice (n=29) based on the experimental design in Extended Data Fig. 2a.

(**b**) Supervised SingleR clustering analysis to identify naive, memory and effector T cell clusters. The pie chart shows the cell number proportion of each cluster.

(**c**) Heat map of row-wise *z*-score-normalized expression for 394 cluster-specific differentially expressed genes used to establish the SingleR clustering in (b). Rows are ordered by hierarchical clustering. Genes for biologically relevant example genes for each cluster are shown.

(**d**) UMAP visualization of unsupervised Seurat clustering analysis of combined 8,198 single memory and effector $CD8^+$ T cell transcriptomes of IL-4Rα^{WT} or IL-4Rα$^{\Delta CD8}$ mice (n=29), based on SingleR clustering in (b). Cluster labels indicate selected differentially expressed genes.

(**e**) Heat map of row-wise *z*-score-normalized expression for 1266 cluster-specific differentially expressed genes used to establish the Seurat clustering analysis in (d). Columns represent the average expression for each cluster.

(**f**) Violin plots show normalized expression in each cluster of 14 cluster-specific signature genes.

Figure 3. Single-cell transcriptomic analysis of spleen T_{VM} upon IL-4 response.

(**a**) Split UMAP visualization of supervised SingleR clustering analysis of combined $CD8^+$ T cell transcriptomes of IL-4Rα^{WT} and IL-4Rα$^{\Delta CD8}$ mice, following treatment with PBS, IL-4c, or *H. polygyrus* infection. Percent of cells in cluster T-memory is indicated for each dataset.

(**b**) Violin plots show normalized expression in the T-memory cluster of selected signature genes. Each dot represents a single cell included in the T-memory cluster and expressing the given gene. The color scale represents the percentage of cells within each cluster expressing the given gene, excluding cells with no expression.

(**c**) Split UMAP visualization of T-memory and T-effector SingleR clustering, highlighting cluster 2 (C2) as identified in Fig. 2d.

(**d**) Scatter plot shows the $\log_2$ fold change of selected biologically relevant genes between IL-4c vs. PBS (x-axis) and *H. polygyrus* vs. PBS (y-axis) mice among cells in cluster 2 from memory/effector SingleR analysis in Fig. 2d. Data are from IL-4Rα^{WT} mice. Each dot represents one gene. The color scale indicates normalized expression. The size of the dot indicates statistical significance.

(**e**) Violin plots show normalized expression in cluster 2 of six selected signature genes. Each dot represents a single cell included in cluster 2 and expressing the given gene. The color

scale represents the percentage of cells within each cluster expressing the given gene, excluding cells with no expression.

Figure 4. Gene expression signature of T_{VM} in the mesLN after helminth infection.

(**a**-**b**) Summary data of total leukocytes, $CD8^+$ T cell numbers and T_{VM} percentages in the spleen (**a**) and mesLN (**b**) at day 15 after *H. polygyrus* infection.

(**c**) Representative contour plots of CD124 expression of concatenated samples, based on the experimental condition. Summary data of median fluorescence intensities (MFI) of EOMES expression in $CD124^+$ or $CD124^-$ cells are shown.

Statistical significance calculated using two-way analysis of variance (ANOVA) and Sidak's multiple comparison-test (***P* < 0.01, ****P* < 0.001, *****P* < 0.0001). Data are representative of three independent experiments with 3-4 mice per group. Mean ± s.e.m., each symbol represents one individual mouse.

(**d**) Split UMAP visualization of combined 6,808 single $CD8^+$ T cell transcriptomes obtained by scRNA-seq analysis of FACsorted then pooled sample tagged $CD124^+$ and $CD124^-$ $CD8^+$ T cells from mesLN of IL-4Rα$^{\Delta CD8}$ mice at day 15 after *H. polygyrus* infection (n=3).

(**e**) UMAP visualization of Seurat clustering analysis. Cluster 5 labels indicate selected differentially expressed genes.

(**f**) Dot plot representation of the top 5 upregulated gene expression in each cluster, based on (f).

(**g**) FeaturePlot representation of selected gene expression in single $CD8^+$ T cells, based on (f).

Figure 5. Specific CD22 expression in IL-4-induced T_{VM}.

(**a**) Feature plot of *Cd22* expression in memory/effector single $CD8^+$ T cell transcriptomes, based on scRNA-seq analysis in Fig. 2d.

(**b**) Representative pseudocolour flow plot of CD22 surface staining on gated T_{VM} from the spleen of WT BALB/c mice at d4 after treatment with IL-4c or at day 15 after infection with *H. polygyrus*. Numbers indicate percent of events in each gate.

(**c**) Imaging cytometry of single splenic $CD8^+$ T cells co-stained for CD3ε, CD8α and CD22 (ImageStream X Mk II; ×60, scale bar, 7 μm)

(**d**) Representative flow cytometry analysis of spleen cells from PBS or IL-4c-treated WT BALB/c mice and stained with anti-CD22. Back-gating of $CD22^+CD8^+$ T cells is shown for CD49d, CD44 and CXCR3 expression. Percentages of $CD22^+$ cells in $CD44^{low}$ T_{NAIVE}, $CD49d^{hi}$ T_{TM}, and T_{VM} are shown. Data are representative of three independent experiments with 4 mice per group (mean ± s.e.m.).

(**e-f**) Summary plots of $CD22^+CD8^+$ T cell counts and percentages in the spleen (**e**) and mesLN (**f**) of IL-4Rα^{WT} or IL-4Rα$^{\Delta CD8}$ mice at day 4 after PBS or IL-4c treatment, or at day 15 after *H. polygyrus* infection. Statistical significance calculated using two-way analysis of variance (ANOVA) and Sidak's multiple comparison-test (**P < 0.01, ***P < 0.001, ****P < 0.0001; comparing IL-4Rα^{WT} and IL-4Rα$^{\Delta CD8}$, and $^{\#\#\#\#}P$ < 0.0001, comparing treated group with WT PBS-treated group). Data are representative of three independent experiments with 3-4 mice per group (mean ± s.e.m.).

(**g**) Representative contour flow plot of CD22 and CD124 co-expression of spleen T_{VM} from IL-4Rα$^{\Delta CD8}$ mice at day 4 after PBS or IL-4c treatment, or at day 15 after *H. polygyrus* infection. Numbers indicate percent of events in each quadrant.

(**h**) Percentages of $CD22^+$ T_{VM} in the spleen and mesLN based on the expression of IL-4Rα at day 4 after PBS or IL-4c treatment, or at day 15 after *H. polygyrus* infection. In IL-4Rα$^{\Delta CD8}$ mice, percentages of $CD22^+$ T_{VM} were reported to $CD124^-$ $CD8^+$ T cells. Data are representative of three independent experiments with 3-4 mice per group (mean ± s.e.m.).

(**i**) Percentages of $CD22^+$ T_{VM} in the spleen of WT and *Il4ra*$^{-/-}$ BALB/c mice, and WT, *Il4ra*$^{-/-}$ and *Stat6*$^{-/-}$ C57BL/6 mice at day 4 after PBS or IL-4c treatment, or at day 15 after *H. polygyrus* infection. Statistical significance calculated using two-way analysis of variance (ANOVA) and Sidak's multiple comparison-test (**P < 0.01, ***P < 0.001, ****P < 0.0001). Data are representative or show pooled data of three independent experiments with 3-4 mice per group (mean ± s.e.m.).

(**j**) Percentages of $CD45.1^+Thy1.2^+$ WT and $CD45.2^+Thy1.2^+$ *Il4ra*$^{-/-}$ cells in the spleen of bone-marrow mixed chimeras, in recipient $CD45.2^+Thy1.1^+$ BALB/c mice and percentages of $CD22^+$ T_{VM} in each $CD45.1^+$ and $CD45.2^+$ compartment of transferred $Thy1.2^+$ cells, at day 4 after PBS or IL-4c treatment, or at day 15 after *H. polygyrus* infection. Statistical significance calculated using two-way analysis of variance (ANOVA) and Sidak's multiple comparison-test (**P < 0.01, ***P < 0.001, ****P < 0.0001). Data are representative of two independent experiments with 3-4 mice per group (mean ± s.e.m.).

Figure 6. $CD22^+$ T_{VM} are transcriptionally distinct from $CD22^-$ T_{VM} and naive T cells.

(**a-d**) WT BALB/c mice were treated with PBS or IL-4c before spleen harvest and purification of $CD44^{low}$ T_{NAIVE} and $CD22^-$ and $CD22^+$ $CD44^{high}CD49d^{low}$ T_{VM} for RNA-seq analysis.

(**a**) Unsupervised hierarchical clustering of the top 250 differentially expressed genes. Specific biologically relevant example genes are listed on the left. Heatmap color scale indicates *z*-score.

(**b**) Heatmap of biologically relevant example gene expression. Color scale indicates normalized mean expression.

(**c**) GSEA enrichment score plots for the indicated KEGG or HALLMARK gene sets between $CD22^-$ and $CD22^+$ T_{VM} in IL-4c treated mice.

(**d**) MA plot of differentially expressed genes between $CD22^-$ and $CD22^+$ T_{VM} in IL-4c treated mice. Each dot represents one gene. Manually curated genes are indicated.

(**e**) Representative flow cytometry analysis of concatenated samples and summary data of the MFI of selected markers in spleen $CD44^{low}$ T_{NAIVE}, $CD22^-$ T_{VM} and $CD22^+$ T_{VM} of IL-4c-treated WT BALB/c mice. Data are representative of three independent experiments with 4-5 mice per group.

(**f**) Representative flow cytometry analysis of concatenated samples revealing IFN-γ expression by eYFP detection in Great reporter C57BL/6 mice (n=3). Numbers in gates indicate mean percent of events (± s.e.m.). Data are representative of two independent experiments.

(**g**) Summary data of IFN-γ^+ ($eYFP^+$) as in (**f**) upon restimulation with PMA and ionomycin or anti-CD3/CD28. Data are representative of two independent experiments.

Statistical significance calculated using two-way analysis of variance (ANOVA) and Sidak's multiple comparison-test (**P < 0.01, ***P < 0.001, ****P < 0.0001).

Figure 7. The TCR repertoire of IL-4-induced $CD22^+$ T_{VM} is diverse but enriched in self-reactive CDR3 sequences.

(**a**) Heatmap of biologically relevant example gene expression from publicly accessible RNA-seq dataset from naive $CD5^+$ and $CD5^-$ T_{VM}[21]. Color scale indicates normalized mean expression.

(**b-h**) $CD44^{low}$ T_{NAIVE}, $CD22^-$ $CD44^{high}CD49d^{low}$ T_{VM} and $CD22^+$ $CD44^{high}CD49d^{low}$ T_{VM} were purified by FACS from the spleen of PBS or IL-4c-treated WT BALB/c mice. CDR3α and CDR3β sequences were extracted from RNA-seq and TCR-seq.

(**b**) Representative tree maps showing CDR3 clonotype usage for the different T cell subsets in PBS- or IL-4c-treated mice; each rectangle represents one CDR3 clonotype and its size corresponds to its relative frequency in the repertoire (rectangle colors are chosen randomly and do not match between plots). Data show CDR3α and CDR3β sequences obtained by TCR-seq.

(**c**) Summary plots of normalized Shannon diversity index of TRA and TRB repertoires for the different T cell subsets in PBS- or IL-4c-treated mice. The normalized index ranges from 0 (no diversity) to 1 (maximal diversity). Each symbol represents an individual mouse. Data show CDR3α and CDR3β sequences obtained by TCR-seq (n=6 in each T cell subset from both conditions (PBS, IL-4c)). Mean ± s.e.m. is indicated. Statistical significance calculated using one-way analysis of variance (ANOVA) and Holm-Sidak's multiple comparison test (ns, not significant, **P < 0.01, ***P < 0.001, ****P < 0.0001).

(**d-e**) Summary plots of hydrophobic doublets in positions 6 and 7 of CDR3α and CDR3β of the different T cell subsets in PBS- or IL-4c-treated mice (**d**) or of paired samples in IL-4c-treated mice (**e**). Each symbol represents an individual mouse, with CDR3 sequences obtained by TCR-seq and RNA-seq (n=10).

(**f-g**) Summary plots of CDR3 strength based on the presence of bulky amino acid side chains for CDR3α and CDR3β in the different T cell subsets in PBS- or IL-4c-treated mice (**f**) or of paired samples in IL-4c-treated mice (**g**). Each symbol represents an individual mouse, with CDR3 sequences obtained by TCR-seq and RNA-seq (n=10).

(**d-g**) Summary data show mean ± s.e.m.. Statistical significance calculated using one-way analysis of variance (ANOVA) and Tukey's multiple comparison test (**d,f**) or one-way analysis of variance (ANOVA) for repeated measures and Dunnett's multiple comparison test (**e,g**), (ns, not significant, $^{**}P < 0.01$, $^{***}P < 0.001$, $^{****}P < 0.0001$).

(**h**) Cumulative contribution of 18 CDR3-derived parameters in principal component analysis for the repertoires of the different T cell subsets in PBS- or IL-4c-treated mice. Plot shows two-dimensional principal component analysis projections of 5,000 functional read sequences of CDR3α and CDR3β that were randomly selected for each of the different samples.

(**i**) Representative flow cytometry analysis and summary data of $CD22^+$ T_{VM} percentages in WT, CSP- or OT-I TCR transgenic mice treated with PBS or IL-4c. Mean ± s.e.m. is indicated (n=4). Statistical significance calculated using two-way analysis of variance (ANOVA) and Sidak multiple comparison test, (ns, not significant, $^{**}P < 0.01$, $^{***}P < 0.001$, $^{****}P < 0.0001$).

Figure 8. The absence of CD22 renders T_{VM} more reactive to helminth infection.

WT, *Cd22*$^{-/-}$ or mixed bone marrow WT: *Cd22*$^{-/-}$ chimeric mice were infected with *H. polygyrus* (200 × L3) by gavage or treated with IL-4c. Analysis was performed at day 15 after *H. polygyrus* infection or at day 4 of IL-4c treatment.

(**a**) *H. polygyrus* adult worm burden in the gut of WT and *Cd22*$^{-/-}$ mice.

(**b**) Fecal egg counts between day 10 and day 14 after infection of WT and *Cd22*$^{-/-}$ mice with *H. polygyrus*.

(**c**) Summary data of $CD22^+$ $CD8^+$ T cell percentages. Bar indicates mean ± s.e.m.

(**d**) Summary data of T_{VM} numbers. Bar indicates mean ± s.e.m.

(**e**) Representative contour and pseudocolour flow plots of spleen $CD8^+$ T cells from mixed bone marrow WT: *Cd22*$^{-/-}$ chimeric mice. Plots show concatenated samples of 4 mice per group, separated by experimental condition. Numbers indicate percent of events in each gate.

(**f**) Summary data of the percentage of T_{VM}, EOMES median fluorescence intensity, percentage of $GZMA^+$ and $CD39^+$ cells in $CD8^+$ T cells from the spleen and mesLN of mixed bone marrow WT: *Cd22*$^{-/-}$ chimeric mice after treatment with IL-4c or infection with *H. polygyrus*.

(**g**) Representative flow cytometry analysis of concatenated $CD8^+$ T cells separated by experimental condition, and summary data of the percentage of IFN-γ^+ and $GZMA^+$ cells in $CD8^+$ T cells following the indicated *ex vivo* restimulation. Numbers indicate percent of events in each gate.

Statistical significance calculated using Mann-Whitney test (**a, b**), two-way analysis of variance (ANOVA) and Sidak's multiple comparison test (**c, d**) or multiple paired *t* test and Sidak multiple comparison test (**f**), (ns, not significant, $^{**}P < 0.01$, $^{***}P < 0.001$, $^{****}P < 0.0001$). Each symbol represents an individual mouse. Data are representative of 3 independent experiments.

Extended Data Figures

Figure S1. Characterization of IL-4Rα$^{\Delta CD8}$ mice.

(**a**) Representative histograms of CD124 expression in the indicated population from the spleen of IL-4Rα^{WT} or IL-4Rα$^{\Delta CD8}$ naive mice.

(**b**) Gating strategy for CD49d^{low}CXCR3^{+} T_{VM} detection.

(**c**) Representative contour flow plot of spleen CD8^{+} T lymphocytes. Numbers indicate percent of events in each gate. Percentages of CD124^{+} and CD124^{-} CD8^{+} T cells in IL-4Rα^{WT} and IL-4Rα$^{\Delta CD8}$ mice.

(**d**) Representative contour plots depicting the gating strategy of CD124^{+} and CD124^{-} CD49d^{low}CXCR3^{+} T_{VM} in the spleen of IL-4Rα^{WT} or IL-4Rα$^{\Delta CD8}$ mice.

(**e**) Representative pseudocolour flow plot of spleen CD8^{+} T lymphocytes. Numbers indicate events percent in each gate.

Statistical significance calculated using Mann-Whitney test (**f**) or two-way analysis of variance (ANOVA) and Sidak's multiple comparison-test (**P < 0.01, ***P < 0.001, ****P < 0.0001). Data are representative of two independent experiments with 4 mice per group. Mean ± s.e.m., each symbol represents one individual mouse.

Figure S2. Single-cell RNA sequencing of spleen CD8^{+} T cells upon IL-4 response.

(**a**) Experimental design of treatment with IL-4c or infection with *H. polygyrus* before CD8^{+} T cell enrichment, hash-tagging, single cell capture, library preparation, and sequencing. The main packages used to analyze scRNA-seq data are listed.

(**b**) Split UMAP visualization of Seurat clustering analysis of combined single CD8^{+} T cell transcriptomes of IL-4Rα^{WT} and IL-4Rα$^{\Delta CD8}$ mice, following treatment with PBS, IL-4c, or *H. polygyrus* infection. (n = 5, except IL-4Rα$^{\Delta CD8}$-PBS (n=4)).

(**c**) Pie charts of cell number proportions of each cluster in each dataset.

(**d**) Box plot distribution of the frequency of each cluster based on the hashtagging of each individual mouse sample included in each dataset.

(**e**) Split UMAP visualization of Seurat clustering analysis as in (b), highlighting cluster 6. The split pie chart shows the cell number proportion of cluster 6 in each dataset.

(**f**) Dot plot showing the average expression levels and percentage of expression of selected genes in each cluster obtained in Fig. 2a.

Figure S3. Single-cell RNA sequencing of spleen memory/effector CD8$^+$ T cells upon IL-4 response.

(**a**) Split UMAP visualization of Seurat clustering analysis of combined single memory/effector CD8$^+$ T cell transcriptomes of IL-4Rα^{WT} and IL-4Rα$^{\Delta CD8}$ mice as in Fig. 2d and following treatment with PBS, IL-4c, or *H. polygyrus* infection. (n = 5, except IL-4Rα$^{\Delta CD8}$-PBS (n=4)).

(**b**) Pie charts of cell number proportions of each cluster in each dataset.

(**c**) Box plot distribution of the frequency of each cluster based on the hashtagging of each individual mouse sample included in each dataset.

(**d**) Split UMAP visualization of Seurat clustering analysis as in (a), highlighting cluster 2. The split pie chart shows the cell number proportion of cluster 2 in each dataset.

Figure S4. Transcription regulation of memory/effector CD8$^+$ T cells upon IL-4 and *H. polygyrus* infection

(**a**) Split UMAP visualization of RNAVelocity trajectory analysis of memory/effector CD8$^+$ T cell transcriptomes of IL-4Rα^{WT} mice.

(**b**) GSEA of the indicated transcription factor in the T_{VM} cluster 2. Top 10 gene set enrichment scores (NES) in scRNA-seq as in Fig. 2.

(**c**) Volcano plot of differentially expressed (DE) genes (P<0.1) showing DE genes in blue from bulk RNAseq data of sorted T_{VM} from PBS- or Sm-treated BALB/c WT mice, obtained in a previously published study[6].

(**d**) Experimental design before CD8$^+$ T cell enrichment, FACsortingand sequencing. UMAP visualizations show FeaturePlots of selected gene expression in single CD8$^+$ T cells from the mesLN of IL-4Rα$^{\Delta CD8}$ mice at day 15 after *H. polygyrus* infection, based on Fig. 3f.

Figure S5. Dynamics of CD22 expression in IL-4-induced T_{VM} during helminth infection.

(**a**) UMAP visualization of concatenated spleen CD8$^+$ T cells analyzed by flow cytometry. FlowSOM clustering analysis was applied based on the fluorescence signals of CD3, CD8, CD44, CXCR3, CD49d, CD124, and CD22. Histograms show the expression levels of the given marker in each cluster.

(**b**) UMAP visualization of concatenated spleen CD8$^+$ T cells analyzed by flow cytometry. Color scale indicates relative expression for each marker.

(**c**) Split UMAP visualization of concatenated spleen CD8$^+$ T cells analyzed by flow cytometry. IL-4Rα negative (CD124$^-$) population is indicated by the dashed area. The area surrounded in red highlights CD22$^+$ events (cluster 0).

(**d**) Representative flow cytometry analysis of concatenated samples (n=5) for CD22 expression in CD4$^+$ and CD8$^+$ T cells in the mesLN of WT C57BL/6 mice at day 15 after *H. polygyrus* infection. Numbers indicate percent of events in each gate.

(**e**) Analysis EOMES expression in $CD22^+CD8^+$ T cells in spleen and mesLN of IL-$4R\alpha^{WT}$ and IL-$4R\alpha^{\Delta CD8}$ BALB/c mice at day 4 after PBS or IL-4c treatment, or at day 15 after *H. polygyrus* infection. Symbols indicate results from each individual mouse.

(**f**) Summary data of T_{VM} and $CD22^+$ T_{VM} percentages and numbers in the spleen of C57BL/6 WT mice at day 15 after *H. polygyrus* infection.

(**g**) $CD22^+$ T_{VM} percentages in the spleen of *H. polygyrus*-infected WT C57BL/6 mice at different time points post-infection.

(**h**) $CD22^+$ T_{VM} percentages in the mesLN, spleen, inguinal LN, and bone marrow of WT C57BL/6 mice at day 15 after *H. polygyrus* infection.

(**i**) Persistence of T_{VM} and $CD22^+$ T_{VM} over time after one i.p. injection of IL-4c and day 0.

(**j**) Percentages and absolute numbers of spleen and thymic $CD22^+$ T cells after IL-4c treatment (2× at 2 days interval, analysis at day 4).

(**k**) WT BALB:B mice were infected with 10^4 PFU of MuHV-4-Luc intranasally, and treated with IL-4c (2× at 2 days interval) at day 30 after infection. Data show representative flow cytometry analysis and summary data of CD22 expression in spleen T_{VM} or in $D^bORF6^{487\text{-}495}$ and $K^bORF61^{524\text{-}531}$ MuHV-4-specific $CD8^+$ T cells. Numbers in gates indicate percentage of tetramer positive events in $CD8^+$ T cells. Scatter plots show mean ± s.e.m. are shown.

Statistical significance calculated using two-way analysis of variance (ANOVA) and Sidak's multiple comparison-test (***P* < 0.01, ****P* < 0.001, *****P* < 0.0001). Data are representative of three independent experiments with 3-5 mice per group (mean ± s.e.m.).

Figure S6. Unconventional activation of $CD22^+$ T_{VM} by IL-4.

(**a**) Principal component analysis of the RNA-seq analysis on sorted $CD44^{low}$ T_{NAIVE} and $CD22^-$ and $CD22^+$ $CD44^{high}CD49d^{low}$ T_{VM} upon PBS or IL-4c treatment.

(**b**) GSEA enrichment score plots for the indicated KEGG gene sets between $CD22^-$ and $CD22^+$ T_{VM} in IL-4c treated mice.

(**c**) Heatmap of Siglec-encoding gene expression in *Mus musculus*. Color scale indicates normalized mean expression.

(**d**) Heatmap of curated T cell exhaustion gene expression. Color scale indicates normalized mean expression.

(**e**) Heatmap of gene expression of killer cell lectin-like receptor subfamily members (*Klr*). Color scale indicates normalized mean expression.

(**f**) Dot plot showing the average expression levels and percentage of expression of selected genes in each cluster from scRNA-seq experiment performed on mesLN $CD124^+$ and $CD124^-$ $CD8^+$ T cells at day 15 after *H. polygyrus* infection, as depicted in Fig. 4 and Extended Data Fig. 4. Selected genes are indicated by blocks based on signature genes identified in bulk

RNA-seq on splenic CD22^{+} T_{VM} after IL-4c treatment, and genes involved in CD22 signaling in B lymphocytes.

Figure S7. Activation of CD22^{+} T_{VM} is IL-4Rα/STAT6-dependent but microbiota independent.

(**a**) Representative flow cytometry analysis of concatenated samples and summary data of the MFI of selected markers in mesLN CD44^{low} T_{NAIVE}, CD22^{-} T_{VM} and CD22^{+} T_{VM} of WT BALB/c mice at day 15 after infection with *H. polygyrus* (n=4-5).

(**b**) Summary data of GATA3^{+} Th2 and T_{VM} responses in mesLN of C57BL/6 WT and *Stat6*$^{-/-}$ mice at day 15 after infection with *H. polygyrus* (pooled data from 3 independent experiments, n=4-5).

(**c**) Representative flow cytometry analysis of concatenated samples for the co-expression of CD22 and GZMA and CD39 in mesLN of C57BL/6 WT and *Stat6*$^{-/-}$ mice at day 15 after infection with *H. polygyrus* (n=5).

(**d**) Representative pseudocolour flow plots of concatenated CD8^{+} T cells from mesLN of IL-4Rα^{WT} and IL-4Rα$^{\Delta CD8}$ BALB/c mice at day 15 after *H. polygyrus* infection. Numbers indicate percent of events in each quadrant (n=5).

(**e**) Representative flow cytometry analysis of concatenated samples revealing CD22 expression by T_{VM}, and coexpression of the indicated markers as shown by the histograms in mesLN of exGF and GF C57BL/6 mice at day 15 after infection with axenic *H. polygyrus* (n=5).

(**f**) Summary data of GATA3^{+} Th2 and T_{VM} responses in mesLN of exGF and GF C57BL/6 mice at day 15 after infection with axenic *H. polygyrus* (pooled data from 3 independent experiments, n=4-5).

Statistical significance calculated using two-way analysis of variance (ANOVA) and Sidak's multiple comparison-test (ns, not significant, $^{**}P < 0.01$, $^{***}P < 0.001$, $^{****}P < 0.0001$). Data are representative of three independent experiments (mean ± s.e.m.).

Figure S8. Diverse TCR repertoire in IL-4-induced CD22^{+} T_{VM} is enriched in self-reactive CDR3 sequences.

CD44^{low} T_{NAIVE}, CD22^{-} CD44^{high}CD49d^{low} T_{VM} and CD22^{+} CD44^{high}CD49d^{low} T_{VM} were purified by FACS from the spleen of PBS or IL-4c-treated WT BALB/c mice. CDR3α and CDR3β sequences were extracted from RNA-seq and TCR-seq.

(**a**) Summary plots of functional CDR3 sequences retrieved from the RNA-seq and TCR-seq experiments. Each symbol represents an individual mouse (n=10).

(**b**) Summary plots of inverse Simpson, Chao1 and efronThisted diversity indexes of TRA and TRB for the different T cell subsets in PBS- or IL-4c-treated mice. Each symbol represents an

individual mouse. Data show CDR3α and CDR3β sequences obtained by TCR-seq. Mean ± s.e.m. is indicated (n=6).

(**c-d**) Summary plots of enrichment of cysteine residues of the central amino acids in CDR3α and CDR3β repertoire of the different T cell subsets in PBS- or IL-4c-treated mice (**d**) or of paired samples in IL-4c-treated mice (**f**).

(**e-f**) Summary plots of CDR3 polarity based on the presence of bulky amino acid side chains of CDR3α and CDR3β repertoire of the different T cell subsets in PBS- or IL-4c-treated mice (**e**) or of paired samples in IL-4c-treated mice (**f**).

(**g-h**) Summary plots of CDR3 volume based on the presence of bulky amino acid side chains of CDR3α and CDR3β of the different T cell subsets in PBS- or IL-4c-treated mice (**g**) or of paired samples in IL-4c-treated mice (**h**).

(**i**) CDR3 physicochemical characteristics used in Fig. 7h.

Statistical significance calculated using one-way analysis of variance (ANOVA) and Holm-Sidak's multiple comparison test. When repeat measurements were analyzed (**d,f,h**), one-way ANOVA for repeated measurements and Dunnett's multiple comparison test was applied. (ns, not significant, $^{**}P < 0.01$, $^{***}P < 0.001$, $^{****}P < 0.0001$).

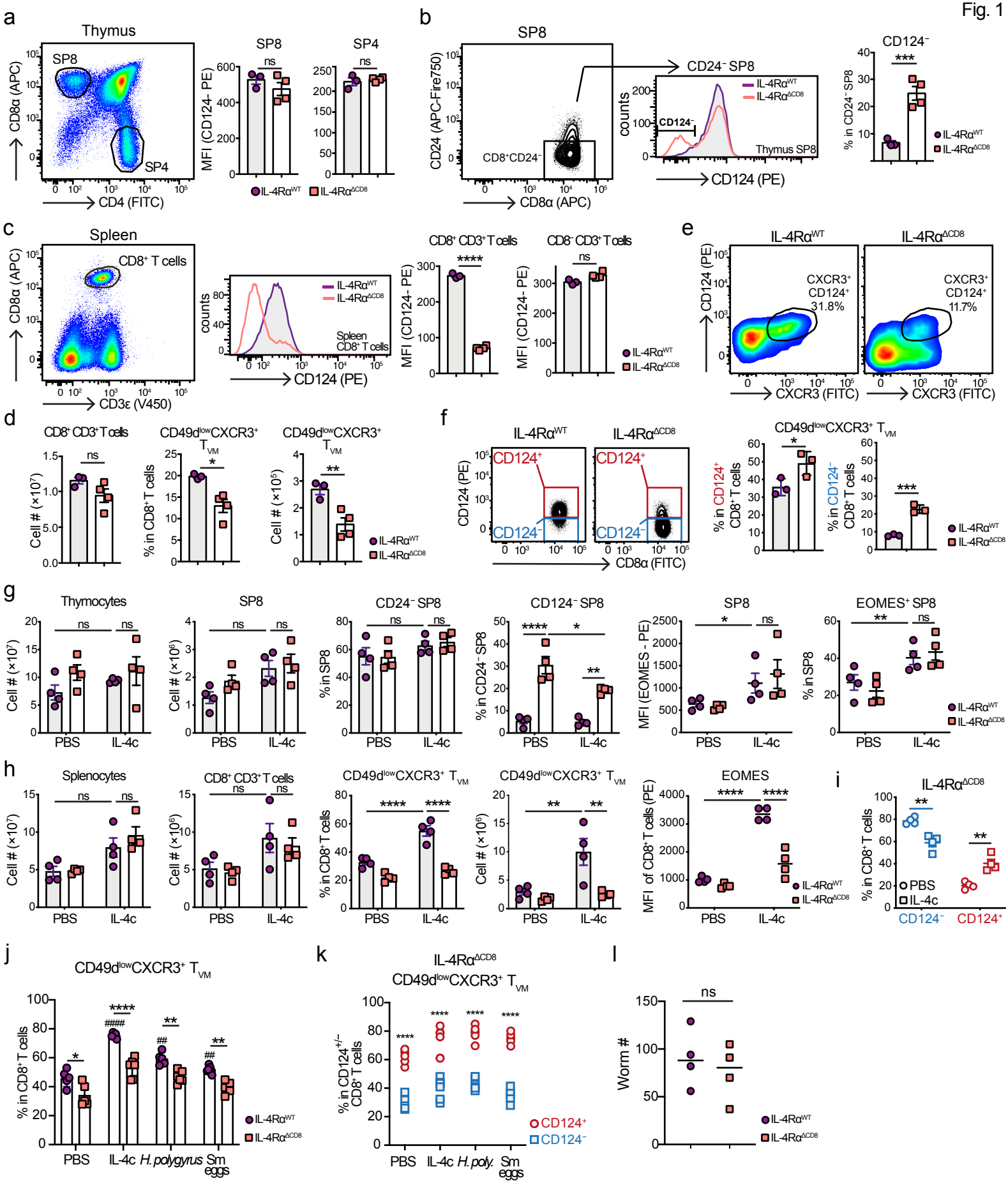
a
Thymus
SP8
SP4
CD8α (APC)
CD4 (FITC)
SP8
SP4
MFI (CD124- PE)
ns
IL-4Rα^WT
IL-4Rα^ΔCD8
b
SP8
CD24 (APC-Fire750)
CD8α (APC)
CD8⁺CD24⁻
CD24⁻ SP8
counts
CD124⁻
Thymus SP8
CD124 (PE)
CD124⁻
% in CD24⁻ SP8
***
c
Spleen
CD8⁺ T cells
CD8α (APC)
CD3ε (V450)
counts
Spleen CD8⁺ T cells
CD124 (PE)
CD8⁺ CD3⁺ T cells
CD8⁻ CD3⁺ T cells
MFI (CD124- PE)
****
e
IL-4Rα^WT
IL-4Rα^ΔCD8
CD124 (PE)
CXCR3⁺ CD124⁺ 31.8%
CXCR3⁺ CD124⁺ 11.7%
CXCR3 (FITC)
d
CD8⁺ CD3⁺ T cells
Cell # (×10⁷)
CD49d^lowCXCR3⁺ T_VM
% in CD8⁺ T cells
Cell # (×10⁵)
f
IL-4Rα^WT
IL-4Rα^ΔCD8
CD124⁺
CD124⁻
CD124 (PE)
CD8α (FITC)
CD49d^lowCXCR3⁺ T_VM
% in CD124⁺ CD8⁺ T cells
% in CD124⁻ CD8⁺ T cells
g
Thymocytes
SP8
CD24⁻ SP8
CD124⁻ SP8
SP8
EOMES⁺ SP8
Cell # (×10⁷)
Cell # (×10⁶)
% in SP8
% in CD24⁻ SP8
MFI (EOMES - PE)
PBS
IL-4c
h
Splenocytes
CD8⁺ CD3⁺ T cells
CD49d^lowCXCR3⁺ T_VM
CD49d^lowCXCR3⁺ T_VM
EOMES
Cell # (×10⁷)
Cell # (×10⁶)
% in CD8⁺ T cells
Cell # (×10⁶)
MFI of CD8⁺ T cells (PE)
i
IL-4Rα^ΔCD8
% in CD8⁺ T cells
PBS
IL-4c
CD124⁻
CD124⁺
j
CD49d^lowCXCR3⁺ T_VM
% in CD8⁺ T cells
PBS
IL-4c
H. polygyrus Sm eggs
k
IL-4Rα^ΔCD8
CD49d^lowCXCR3⁺ T_VM
% in CD124^+/- CD8⁺ T cells
CD124⁺
CD124⁻
PBS
IL-4c
H. poly. Sm eggs
l
Worm #
ns

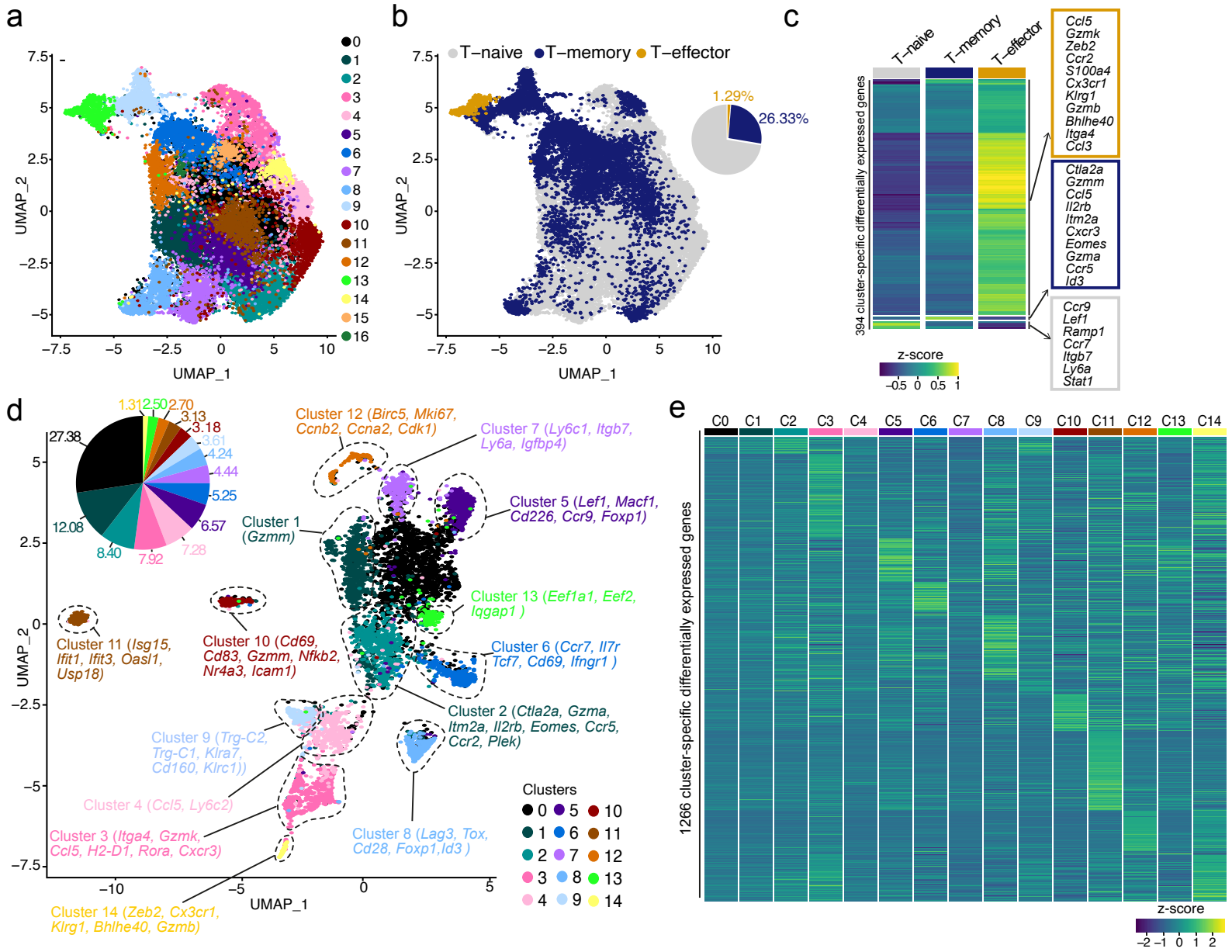
a
b
c
UMAP_1
UMAP_2
T−naive
T−memory
T−effector
1.29%
26.33%
394 cluster-specific differentially expressed genes
z-score
Ccl5 Gzmk Zeb2 Ccr2 S100a4 Cx3cr1 Klrg1 Gzmb Bhlhe40 Itga4 Ccl3
Ctla2a Gzmm Ccl5 Il2rb Itm2a Cxcr3 Eomes Gzma Ccr5 Id3
Ccr9 Lef1 Ramp1 Ccr7 Itgb7 Ly6a Stat1

d
Cluster 12 (Birc5, Mki67, Ccnb2, Ccna2, Cdk1)
Cluster 7 (Ly6c1, Itgb7, Ly6a, Igfbp4)
Cluster 5 (Lef1, Macf1, Cd226, Ccr9, Foxp1)
Cluster 1 (Gzmm)
Cluster 13 (Eef1a1, Eef2, Iqgap1)
Cluster 11 (Isg15, Ifit1, Ifit3, Oasl1, Usp18)
Cluster 10 (Cd69, Cd83, Gzmm, Nfkb2, Nr4a3, Icam1)
Cluster 6 (Ccr7, Il7r Tcf7, Cd69, Ifngr1)
Cluster 2 (Ctla2a, Gzma, Itm2a, Il2rb, Eomes, Ccr5, Ccr2, Plek)
Cluster 9 (Trg-C2, Trg-C1, Klra7, Cd160, Klrc1))
Cluster 4 (Ccl5, Ly6c2)
Cluster 3 (Itga4, Gzmk, Ccl5, H2-D1, Rora, Cxcr3)
Cluster 8 (Lag3, Tox, Cd28, Foxp1,Id3)
Cluster 14 (Zeb2, Cx3cr1, Klrg1, Bhlhe40, Gzmb)
Clusters
UMAP_1
UMAP_2

e
1266 cluster-specific differentially expressed genes
z-score

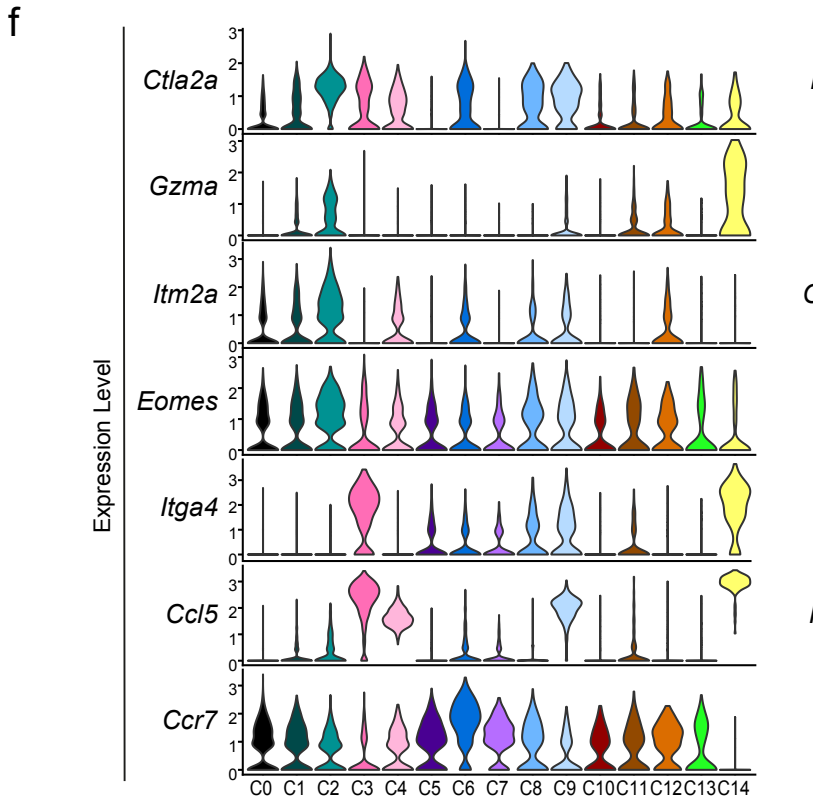
f
Ctla2a
Gzma
Itm2a
Eomes
Itga4
Ccl5
Ccr7
Expression Level

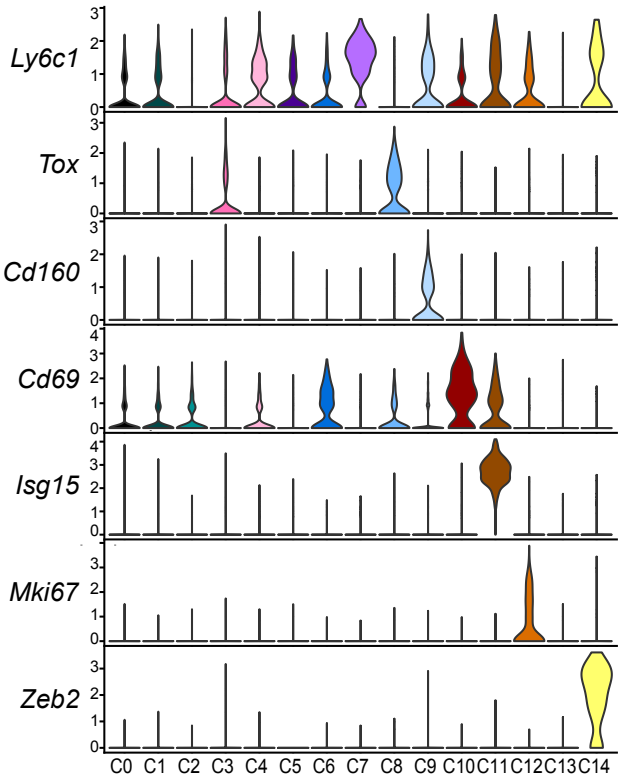
Ly6c1
Tox
Cd160
Cd69
Isg15
Mki67
Zeb2

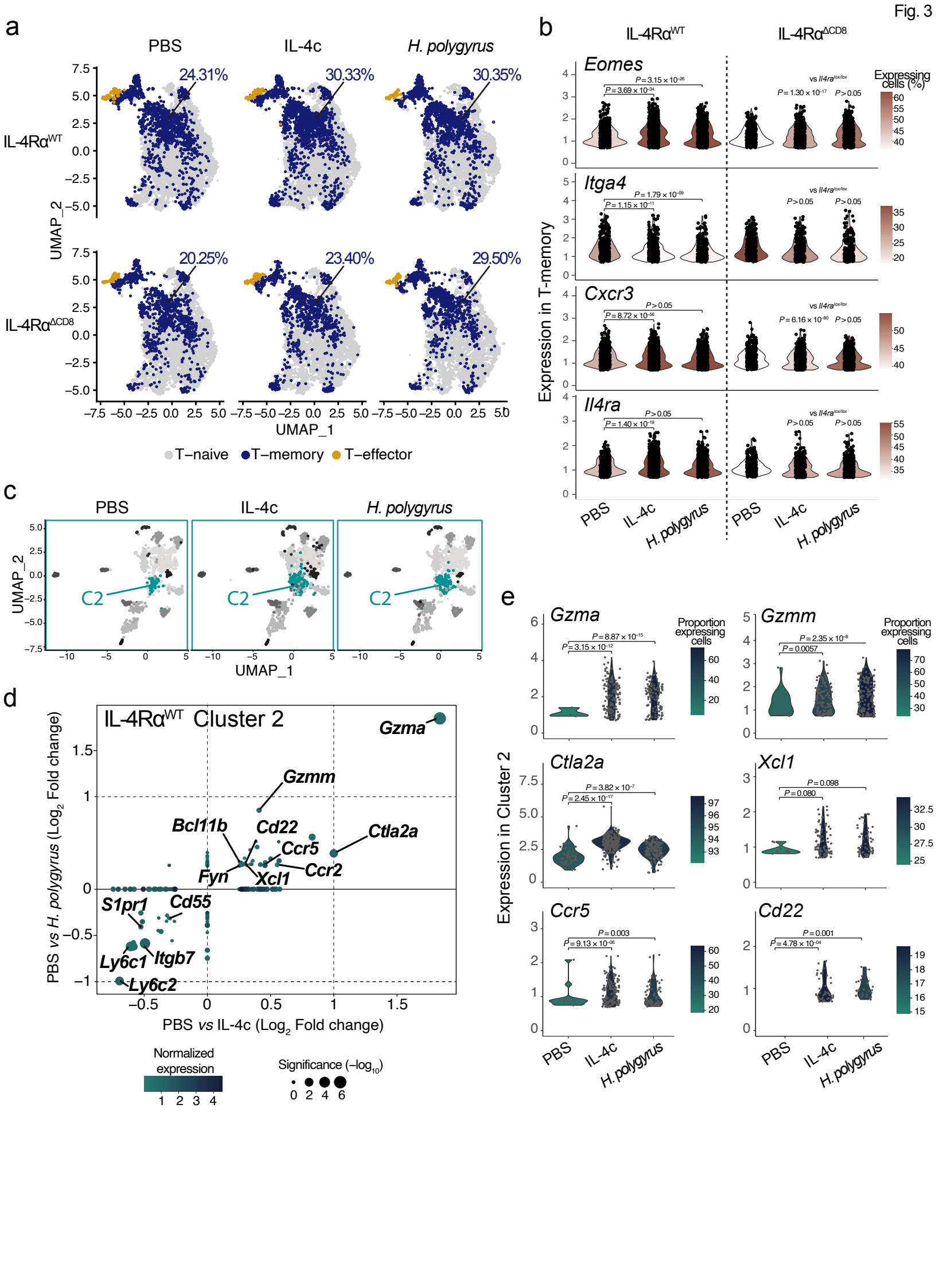
a
PBS
IL-4c
H. polygyrus
24.31%
30.33%
30.35%
20.25%
23.40%
29.50%
IL-4Rα^WT
IL-4Rα^ΔCD8
UMAP_2
UMAP_1
T−naive
T−memory
T−effector
b
IL-4Rα^WT
IL-4Rα^ΔCD8
Eomes
Itga4
Cxcr3
Il4ra
Expression in T-memory
Expressing cells (%)
PBS
IL-4c
H. polygyrus
c
PBS
IL-4c
H. polygyrus
C2
UMAP_2
UMAP_1
d
IL-4Rα^WT Cluster 2
Gzma
Gzmm
Bcl11b
Cd22
Ctla2a
Ccr5
Ccr2
Fyn
Xcl1
S1pr1
Cd55
Ly6c1
Itgb7
Ly6c2
PBS vs H. polygyrus (Log2 Fold change)
PBS vs IL-4c (Log2 Fold change)
Normalized expression
Significance (−log10)
e
Gzma
Gzmm
Ctla2a
Xcl1
Ccr5
Cd22
Expression in Cluster 2
Proportion expressing cells
PBS
IL-4c
H. polygyrus

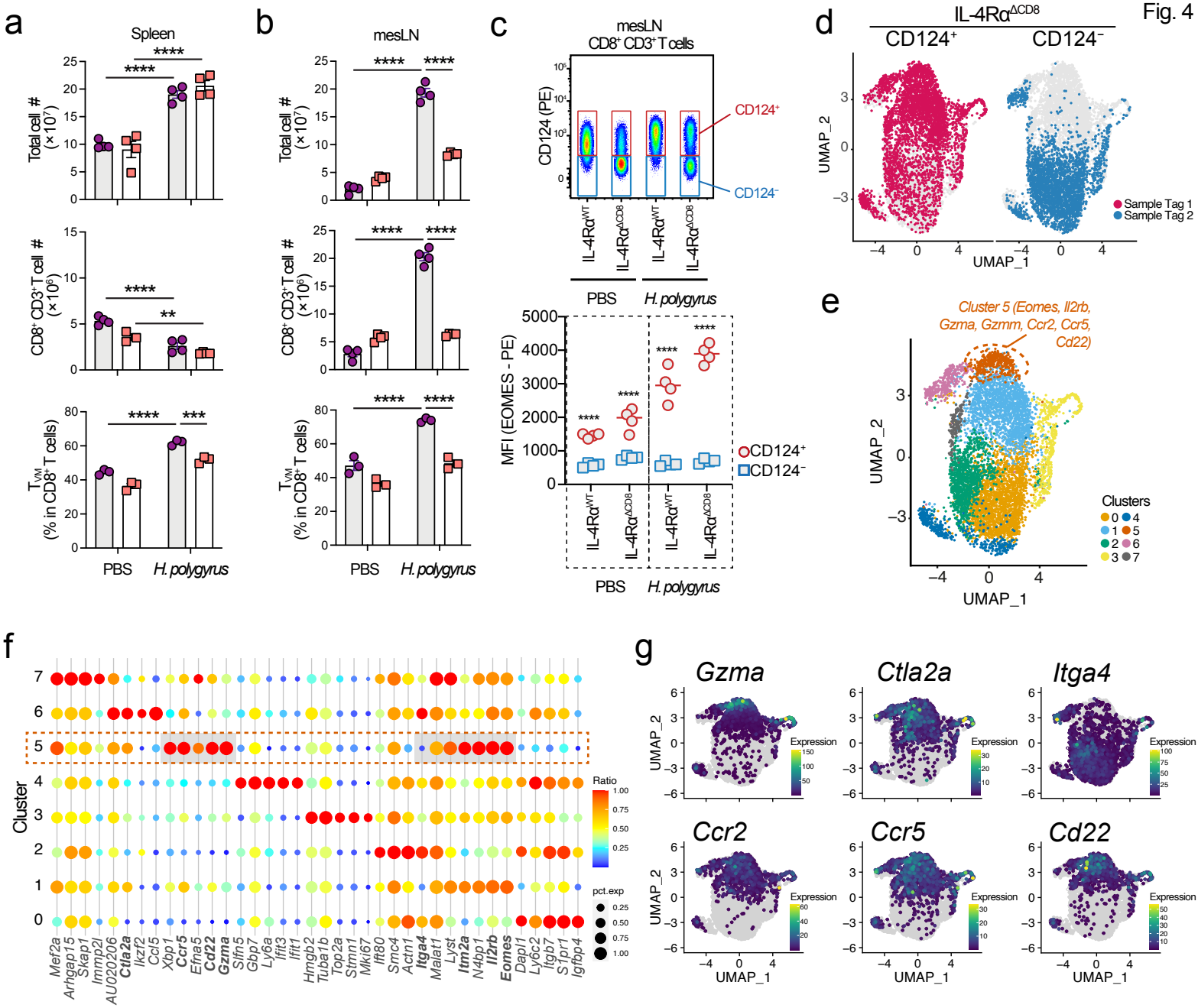
a
Spleen
Total cell # (×10⁷)
CD8⁺ CD3⁺ T cell # (×10⁶)
T_VM (% in CD8⁺ T cells)
PBS
H. polygyrus
b
mesLN
c
mesLN
CD8⁺ CD3⁺ T cells
CD124 (PE)
CD124⁺
CD124⁻
IL-4Rα^WT
IL-4Rα^ΔCD8
MFI (EOMES - PE)
d
IL-4Rα^ΔCD8
CD124⁺
CD124⁻
UMAP_2
UMAP_1
Sample Tag 1
Sample Tag 2
e
Cluster 5 (Eomes, Il2rb, Gzma, Gzmm, Ccr2, Ccr5, Cd22)
Clusters
f
Cluster
Ratio
pct.exp
Mef2a
Arhgap15
Skap1
Immp2l
AU020206
Ctla2a
Ikzf2
Ccl5
Xbp1
Ccr5
Efna5
Cd22
Gzma
Slfn5
Gbp7
Ly6a
Ifit3
Ifit1
Hmgb2
Tuba1b
Top2a
Stmn1
Mki67
Ift80
Smc4
Actn1
Itga4
Malat1
Lyst
Itm2a
N4bp1
Il2rb
Eomes
Dapl1
Ly6c2
Itgb7
S1pr1
Igfbp4
g
Gzma
Ctla2a
Itga4
Ccr2
Ccr5
Cd22
Expression

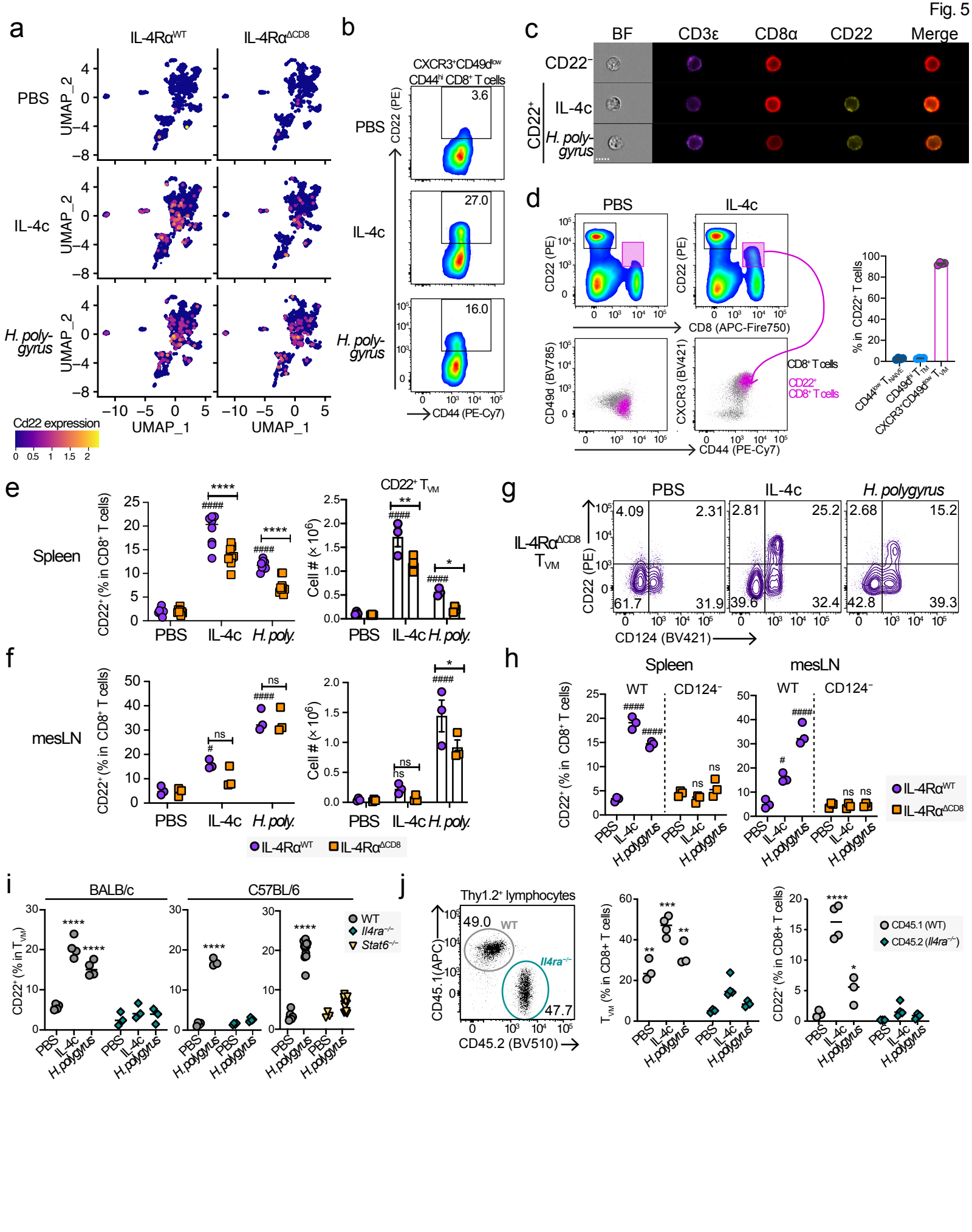
a
IL-4Rα^WT
IL-4Rα^ΔCD8
PBS
IL-4c
H. poly-gyrus
UMAP_2
UMAP_1
Cd22 expression
b
CXCR3+CD49dlow CD44hi CD8+ T cells
CD22 (PE)
CD44 (PE-Cy7)
3.6
27.0
16.0
c
BF
CD3ε
CD8α
CD22
Merge
CD22−
CD22+
IL-4c
H. poly-gyrus
d
PBS
IL-4c
CD22 (PE)
CD8 (APC-Fire750)
CD49d (BV785)
CXCR3 (BV421)
CD44 (PE-Cy7)
CD8+ T cells
CD22+ CD8+ T cells
% in CD22+ T cells
CD44low TNAIVE
CD49dhi TTM
CXCR3+CD49dlow TVM
e
Spleen
CD22+ (% in CD8+ T cells)
CD22+ TVM
Cell # (× 10^6)
PBS
IL-4c
H. poly.
f
mesLN
CD22+ (% in CD8+ T cells)
Cell # (× 10^6)
ns
IL-4Rα^WT
IL-4Rα^ΔCD8
g
PBS
IL-4c
H. polygyrus
IL-4Rα^ΔCD8 TVM
CD22 (PE)
CD124 (BV421)
4.09
2.31
61.7
31.9
2.81
25.2
39.6
32.4
2.68
15.2
42.8
39.3
h
Spleen
mesLN
WT
CD124−
CD22+ (% in CD8+ T cells)
IL-4Rα^WT
IL-4Rα^ΔCD8
i
BALB/c
C57BL/6
CD22+ (% in TVM)
WT
Il4ra−/−
Stat6−/−
j
Thy1.2+ lymphocytes
CD45.1(APC)
CD45.2 (BV510)
49.0
WT
Il4ra−/−
47.7
TVM (% in CD8+ T cells)
CD22+ (% in CD8+ T cells)
CD45.1 (WT)
CD45.2 (Il4ra−/−)

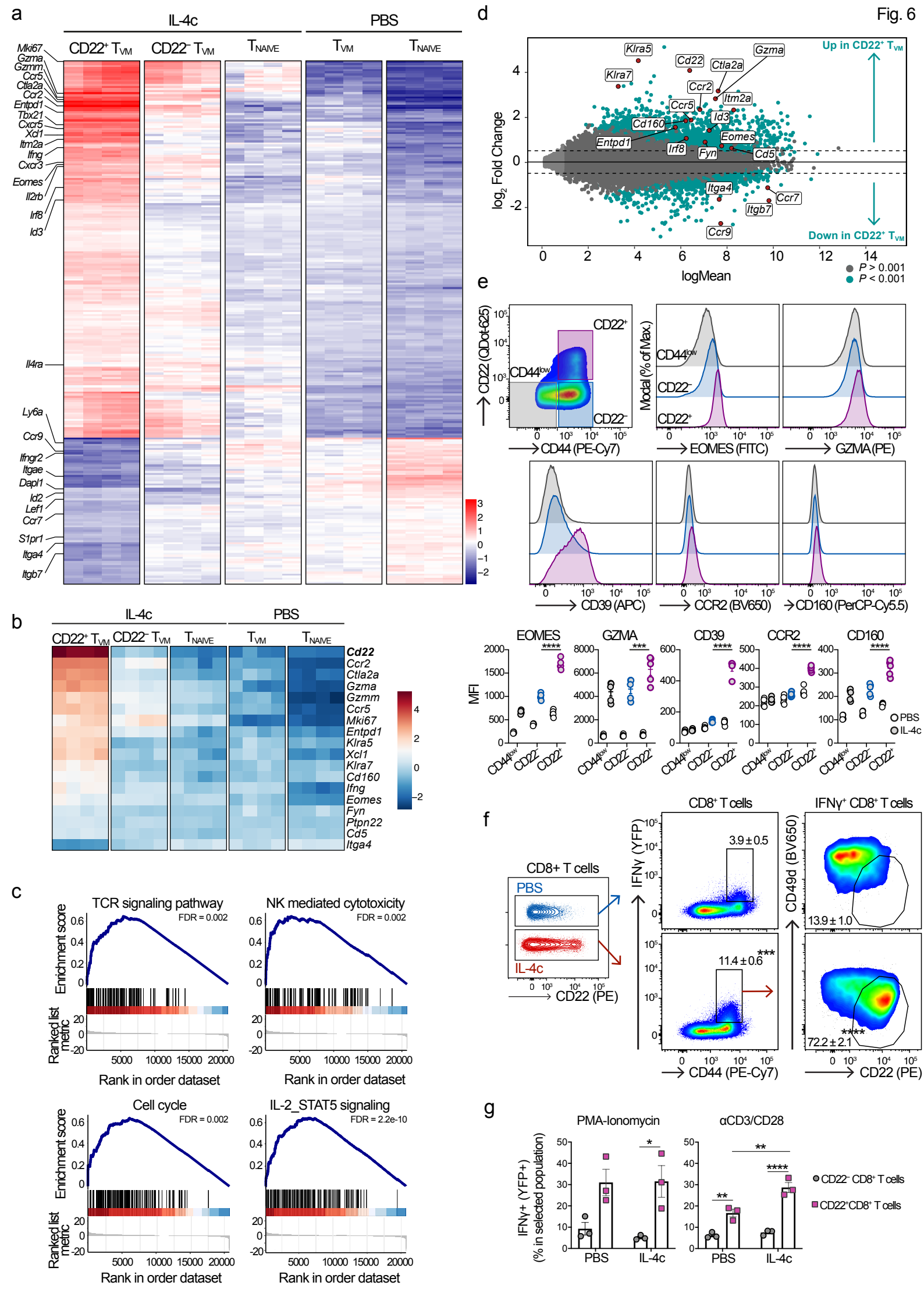
a
IL-4c
PBS
CD22+ TVM
CD22- TVM
TNAIVE
TVM
TNAIVE
Mki67
Gzma
Gzmm
Ccr5
Ctla2a
Ccr2
Entpd1
Tbx21
Cxcr5
Xcl1
Itm2a
Ifng
Cxcr3
Eomes
Il2rb
Irf8
Id3
Il4ra
Ly6a
Ccr9
Ifngr2
Itgae
Dapl1
Id2
Lef1
Ccr7
S1pr1
Itga4
Itgb7
b
IL-4c
PBS
CD22+ TVM
CD22- TVM
TNAIVE
TVM
TNAIVE
Cd22
Ccr2
Ctla2a
Gzma
Gzmm
Ccr5
Mki67
Entpd1
Klra5
Xcl1
Klra7
Cd160
Ifng
Eomes
Fyn
Ptpn22
Cd5
Itga4
c
TCR signaling pathway
FDR = 0.002
NK mediated cytotoxicity
FDR = 0.002
Cell cycle
FDR = 0.002
IL-2_STAT5 signaling
FDR = 2.2e-10
Enrichment score
Ranked list metric
Rank in order dataset
d
Klra5
Cd22
Gzma
Ctla2a
Klra7
Ccr2
Itm2a
Ccr5
Id3
Cd160
Entpd1
Irf8
Fyn
Eomes
Cd5
Itga4
Ccr7
Itgb7
Ccr9
Up in CD22+ TVM
Down in CD22+ TVM
log2 Fold Change
logMean
P > 0.001
P < 0.001
e
CD22 (QDot-625)
CD22+
CD44low
CD22-
CD44 (PE-Cy7)
Modal (% of Max.)
CD44low
CD22-
CD22+
EOMES (FITC)
GZMA (PE)
CD39 (APC)
CCR2 (BV650)
CD160 (PerCP-Cy5.5)
EOMES
GZMA
CD39
CCR2
CD160
MFI
PBS
IL-4c
CD44low
CD22-
CD22+
f
CD8+ T cells
PBS
IL-4c
CD22 (PE)
IFNγ (YFP)
3.9 ± 0.5
11.4 ± 0.6
CD44 (PE-Cy7)
CD8+ T cells
IFNγ+ CD8+ T cells
CD49d (BV650)
13.9 ± 1.0
72.2 ± 2.1
CD22 (PE)
g
PMA-Ionomycin
αCD3/CD28
IFNγ+ (YFP+) (% in selected population)
PBS
IL-4c
PBS
IL-4c
CD22- CD8+ T cells
CD22+CD8+ T cells

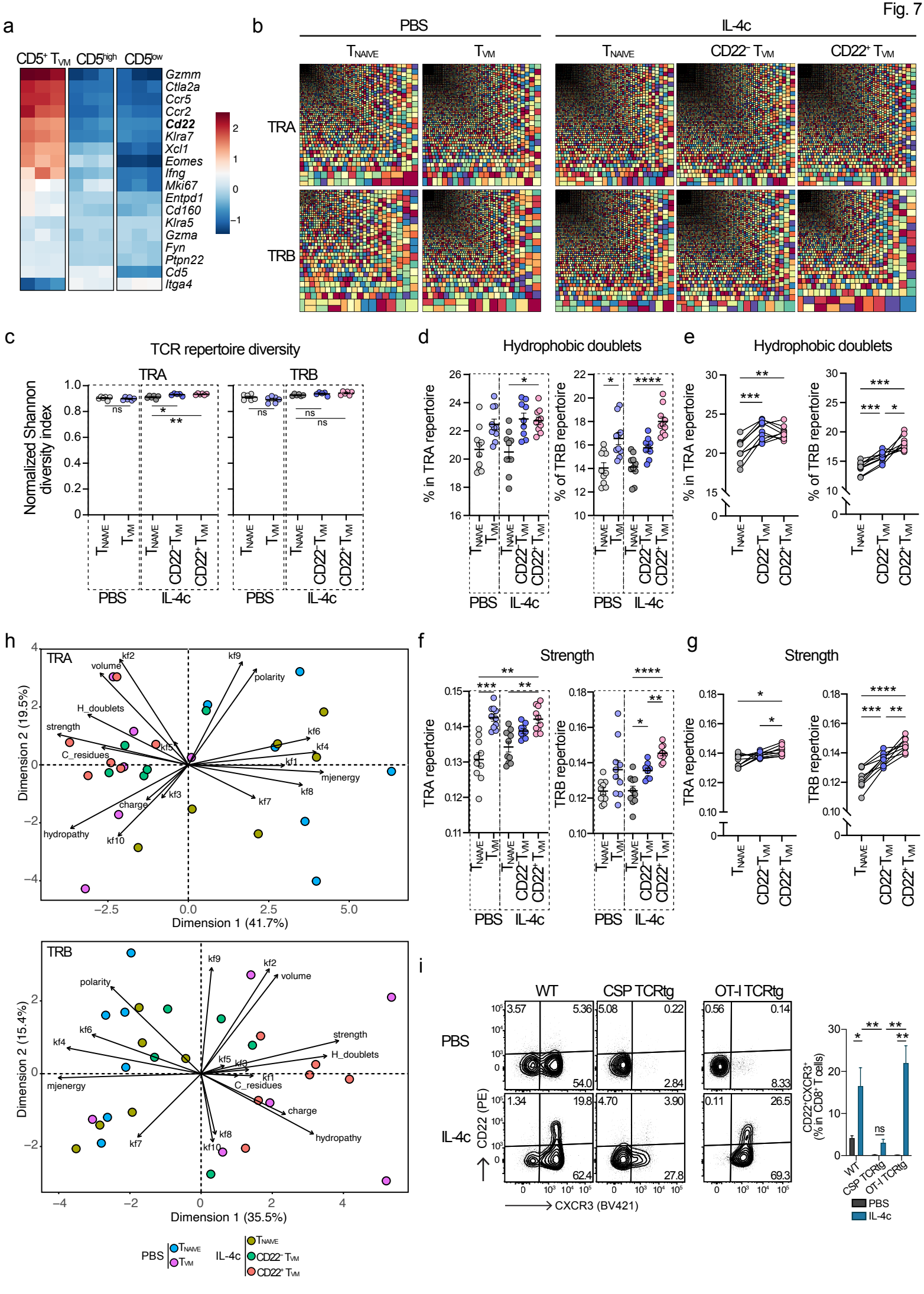
a
CD5+ TVM
CD5high
CD5low
Gzmm
Ctla2a
Ccr5
Ccr2
Cd22
Klra7
Xcl1
Eomes
Ifng
Mki67
Entpd1
Cd160
Klra5
Gzma
Fyn
Ptpn22
Cd5
Itga4
b
PBS
IL-4c
TNAIVE
TVM
CD22− TVM
CD22+ TVM
TRA
TRB
c
TCR repertoire diversity
Normalized Shannon diversity index
d
Hydrophobic doublets
% in TRA repertoire
% of TRB repertoire
e
Hydrophobic doublets
f
Strength
TRA repertoire
TRB repertoire
g
Strength
h
TRA
TRB
Dimension 1 (41.7%)
Dimension 2 (19.5%)
Dimension 1 (35.5%)
Dimension 2 (15.4%)
volume
polarity
H_doublets
strength
C_residues
mjenergy
charge
hydropathy
i
WT
CSP TCRtg
OT-I TCRtg
CD22 (PE)
CXCR3 (BV421)
CD22+CXCR3+ (% in CD8+ T cells)

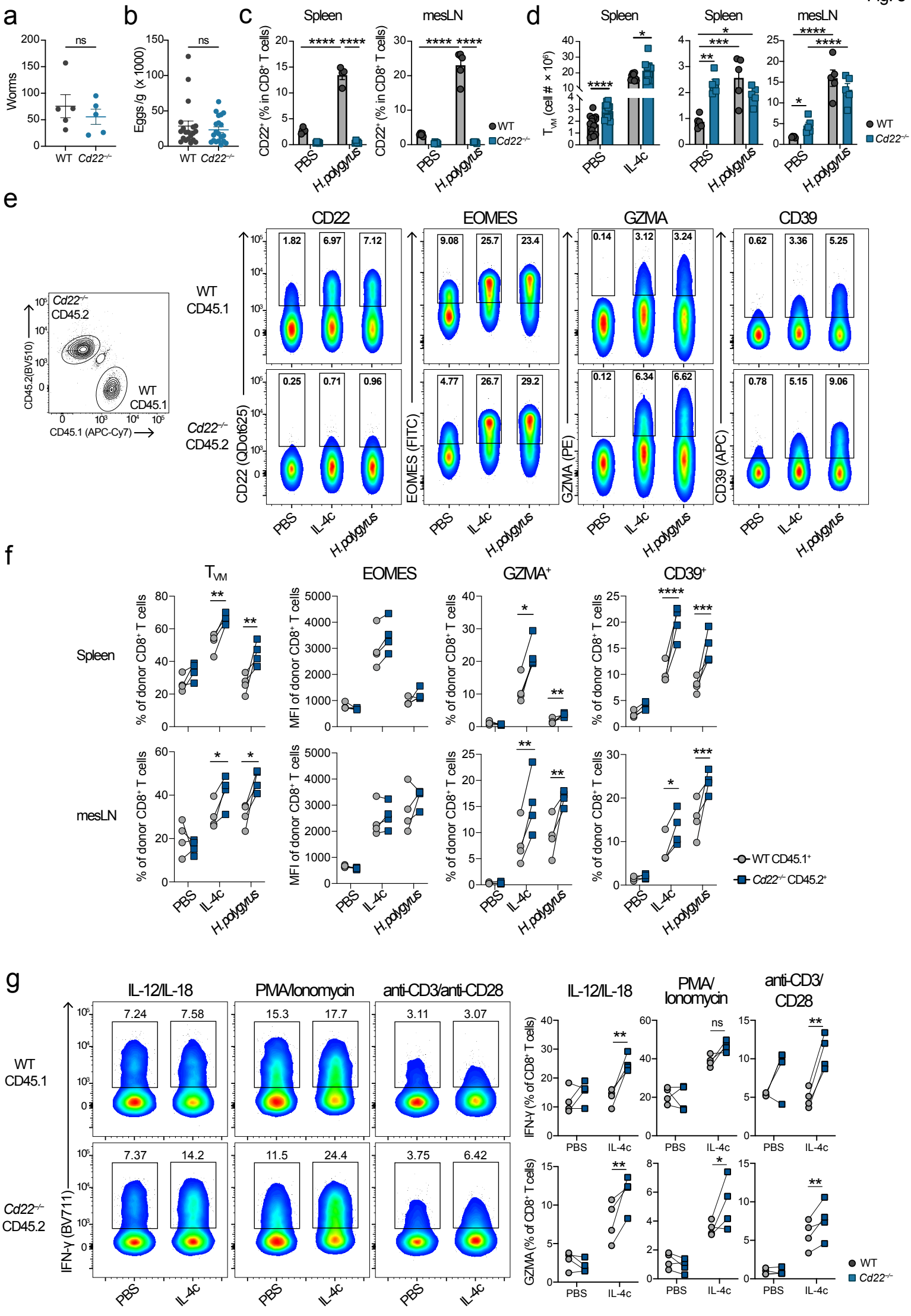
a
Worms
ns
WT
Cd22−/−
b
Eggs/g (x 1000)
ns
WT
Cd22−/−
c
Spleen
mesLN
CD22+ (% in CD8+ T cells)
PBS
H.polygyrus
WT
Cd22−/−
d
Spleen
mesLN
TVM (cell # × 10^6)
PBS
IL-4c
H.polygyrus
WT
Cd22−/−
e
CD22
EOMES
GZMA
CD39
Cd22−/− CD45.2
WT CD45.1
CD45.2(BV510)
CD45.1 (APC-Cy7)
CD22 (QDot625)
EOMES (FITC)
GZMA (PE)
CD39 (APC)
1.82
6.97
7.12
9.08
25.7
23.4
0.14
3.12
3.24
0.62
3.36
5.25
0.25
0.71
0.96
4.77
26.7
29.2
0.12
6.34
6.62
0.78
5.15
9.06
PBS
IL-4c
H.polygyrus
f
TVM
EOMES
GZMA+
CD39+
Spleen
mesLN
% of donor CD8+ T cells
MFI of donor CD8+ T cells
PBS
IL-4c
H.polygyrus
WT CD45.1+
Cd22−/− CD45.2+
g
IL-12/IL-18
PMA/Ionomycin
anti-CD3/anti-CD28
WT CD45.1
Cd22−/− CD45.2
IFN-γ (BV711)
7.24
7.58
15.3
17.7
3.11
3.07
7.37
14.2
11.5
24.4
3.75
6.42
PBS
IL-4c
IFN-γ (% of CD8+ T cells)
GZMA (% of CD8+ T cells)
ns
WT
Cd22−/−

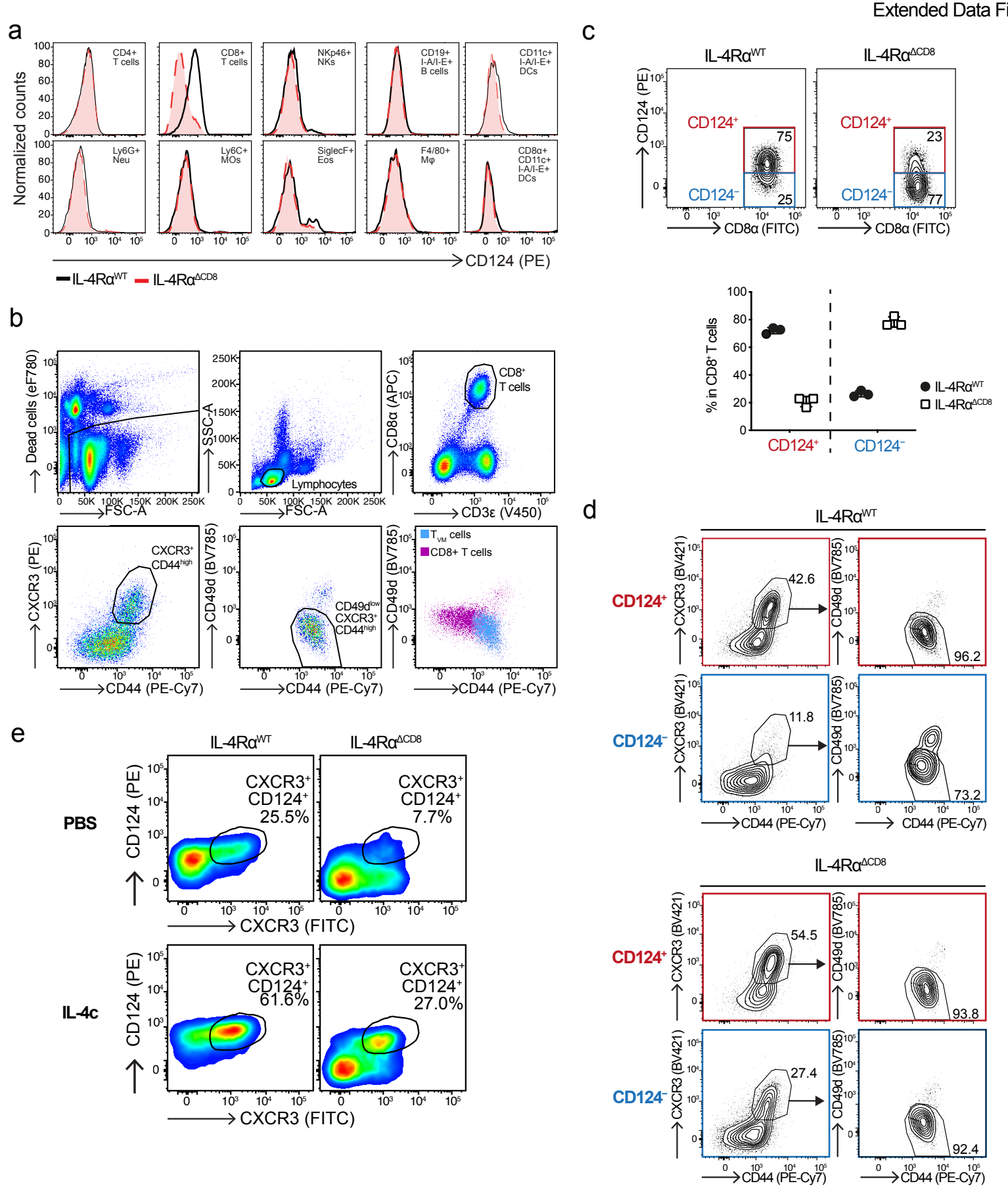
a
Normalized counts
CD4+ T cells
CD8+ T cells
NKp46+ NKs
CD19+ I-A/I-E+ B cells
CD11c+ I-A/I-E+ DCs
Ly6G+ Neu
Ly6C+ MOs
SiglecF+ Eos
F4/80+ Mφ
CD8α+ CD11c+ I-A/I-E+ DCs
CD124 (PE)
IL-4Rα^WT
IL-4Rα^ΔCD8
b
Dead cells (eF780)
FSC-A
SSC-A
Lymphocytes
CD8α (APC)
CD8+ T cells
CD3ε (V450)
CXCR3 (PE)
CXCR3+ CD44high
CD49d (BV785)
CD49dlow CXCR3+ CD44high
CD44 (PE-Cy7)
TVM cells
CD8+ T cells
c
IL-4Rα^WT
IL-4Rα^ΔCD8
CD124 (PE)
CD124+
CD124−
75
25
23
77
CD8α (FITC)
% in CD8+ T cells
d
IL-4Rα^WT
IL-4Rα^ΔCD8
CD124+
CD124−
CXCR3 (BV421)
CD49d (BV785)
42.6
96.2
11.8
73.2
54.5
93.8
27.4
92.4
CD44 (PE-Cy7)
e
IL-4Rα^WT
IL-4Rα^ΔCD8
PBS
IL-4c
CD124 (PE)
CXCR3+ CD124+ 25.5%
CXCR3+ CD124+ 7.7%
CXCR3+ CD124+ 61.6%
CXCR3+ CD124+ 27.0%
CXCR3 (FITC)

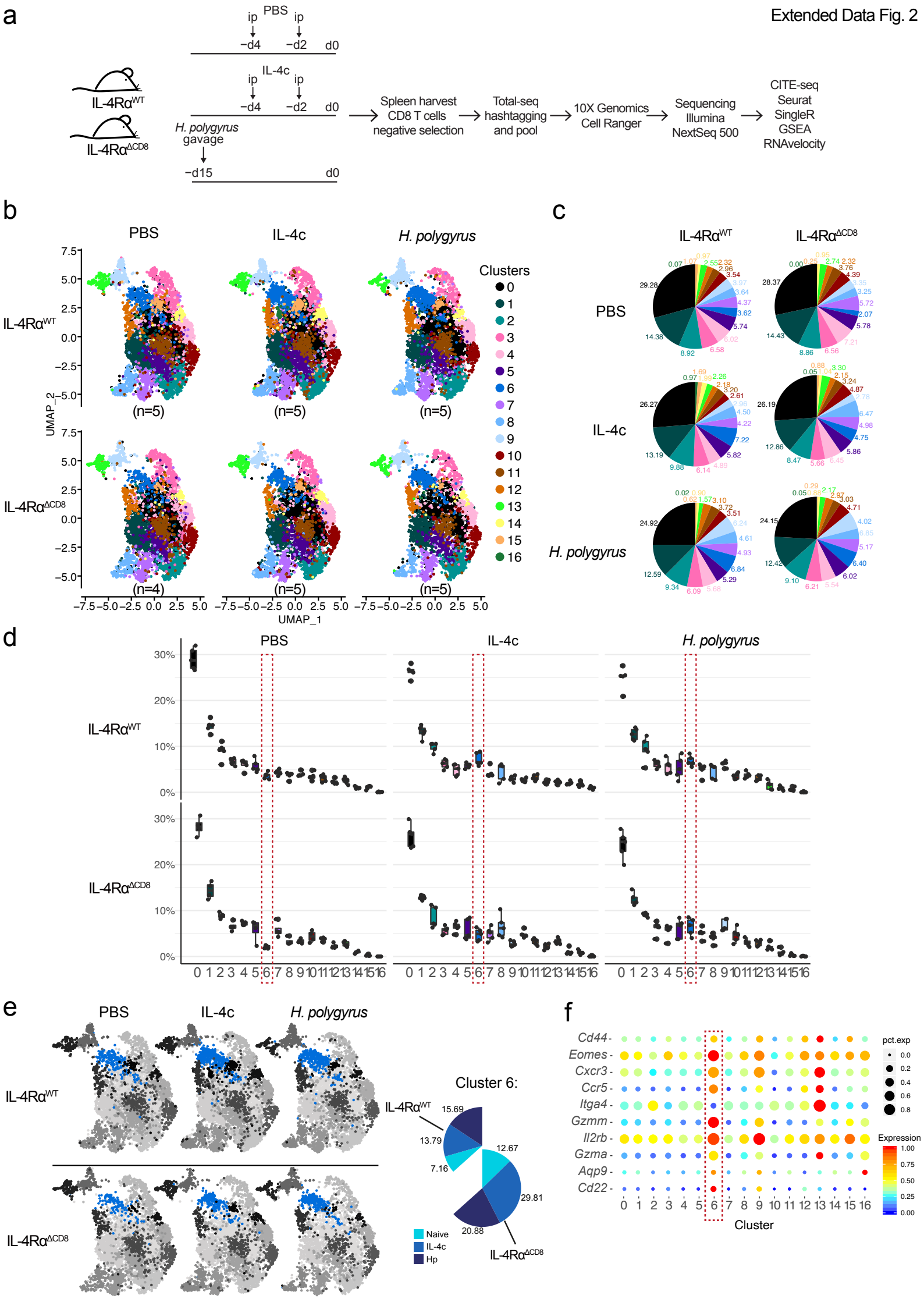
a
PBS
ip
ip
−d4
−d2
d0
IL-4c
ip
ip
−d4
−d2
d0
IL-4Rα^WT
IL-4Rα^ΔCD8
H. polygyrus
gavage
−d15
d0
Spleen harvest
CD8 T cells
negative selection
Total-seq
hashtagging
and pool
10X Genomics
Cell Ranger
Sequencing
Illumina
NextSeq 500
CITE-seq
Seurat
SingleR
GSEA
RNAvelocity
b
PBS
IL-4c
H. polygyrus
IL-4Rα^WT
IL-4Rα^ΔCD8
UMAP_2
UMAP_1
(n=5)
(n=4)
Clusters
0
1
2
3
4
5
6
7
8
9
10
11
12
13
14
15
16
c
IL-4Rα^WT
IL-4Rα^ΔCD8
PBS
IL-4c
H. polygyrus
d
PBS
IL-4c
H. polygyrus
IL-4Rα^WT
IL-4Rα^ΔCD8
30%
20%
10%
0%
0 1 2 3 4 5 6 7 8 9 10 11 12 13 14 15 16
e
PBS
IL-4c
H. polygyrus
IL-4Rα^WT
IL-4Rα^ΔCD8
Cluster 6:
IL-4Rα^WT
15.69
13.79
12.67
7.16
29.81
20.88
IL-4Rα^ΔCD8
Naive
IL-4c
Hp
f
Cd44
Eomes
Cxcr3
Ccr5
Itga4
Gzmm
Il2rb
Gzma
Aqp9
Cd22
0 1 2 3 4 5 6 7 8 9 10 11 12 13 14 15 16
Cluster
pct.exp
0.0
0.2
0.4
0.6
0.8
Expression
1.00
0.75
0.50
0.25
0.00

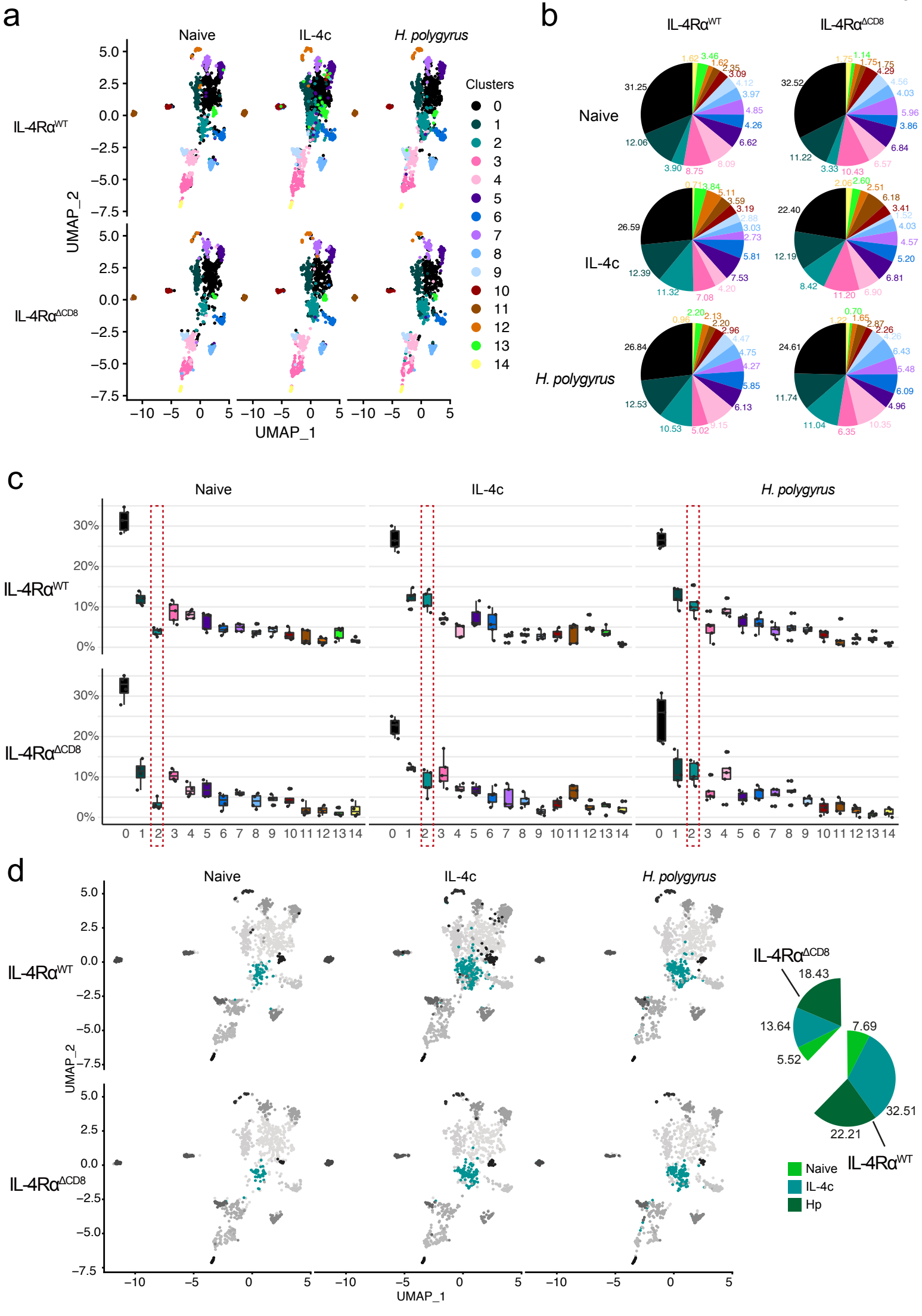
a
Naive
IL-4c
H. polygyrus
IL-4Rα^WT
IL-4Rα^ΔCD8
UMAP_2
UMAP_1
Clusters
0
1
2
3
4
5
6
7
8
9
10
11
12
13
14
b
IL-4Rα^WT
IL-4Rα^ΔCD8
Naive
IL-4c
H. polygyrus
c
Naive
IL-4c
H. polygyrus
IL-4Rα^WT
IL-4Rα^ΔCD8
d
Naive
IL-4c
H. polygyrus
IL-4Rα^WT
IL-4Rα^ΔCD8
UMAP_2
UMAP_1
IL-4Rα^ΔCD8
18.43
13.64
7.69
5.52
32.51
22.21
IL-4Rα^WT
Naive
IL-4c
Hp

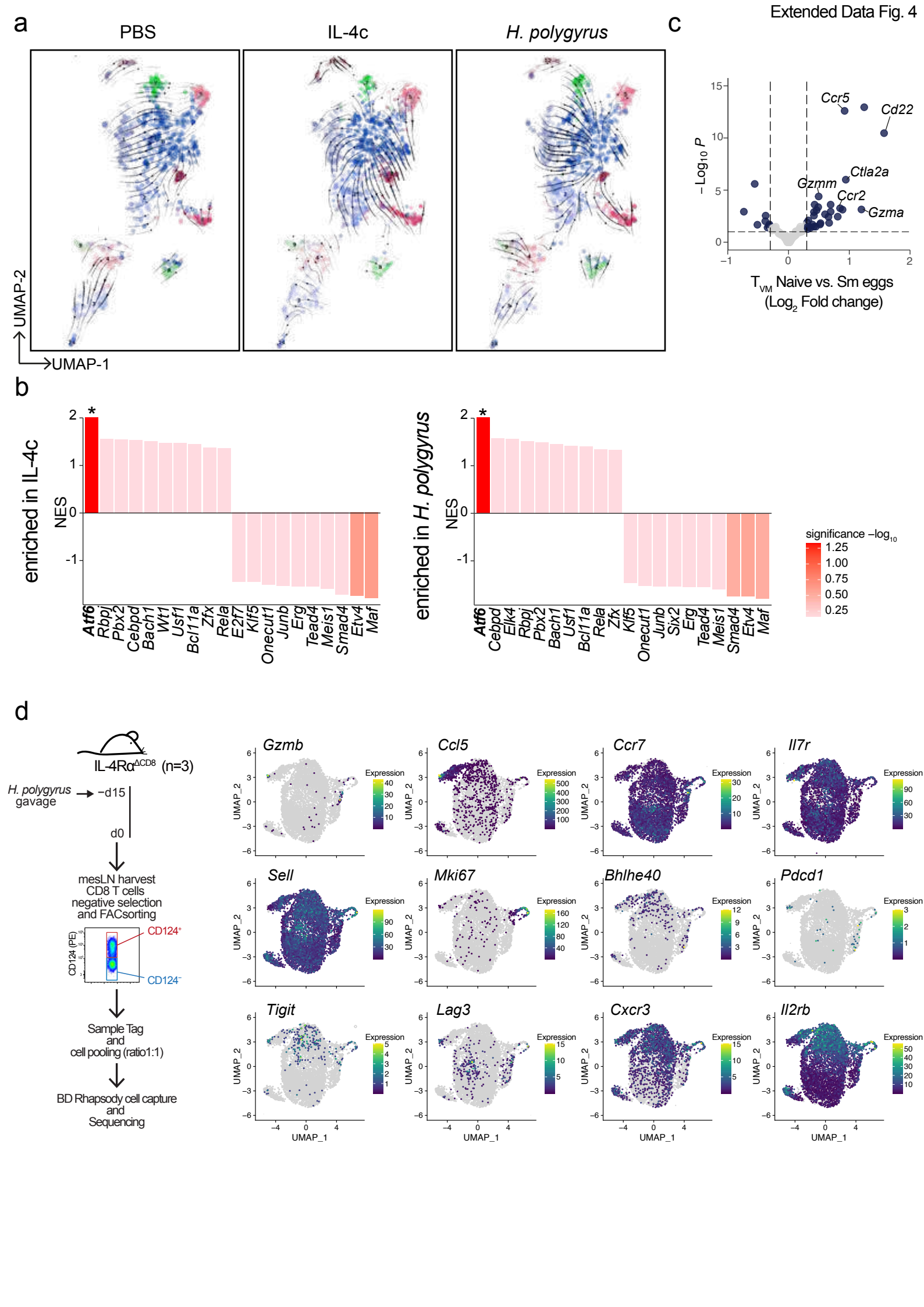
a
PBS
IL-4c
H. polygyrus
UMAP-2
UMAP-1
c
Ccr5
Cd22
Ctla2a
Gzmm
Ccr2
Gzma
−Log10 P
TVM Naive vs. Sm eggs
(Log2 Fold change)
b
enriched in IL-4c
NES
Atf6 Rbpj Pbx2 Cebpd Bach1 Wt1 Usf1 Bcl11a Zfx Rela E2f7 Klf5 Onecut1 Junb Erg Tead4 Meis1 Smad4 Etv4 Maf
enriched in H. polygyrus
Atf6 Cebpd Elk4 Rbpj Pbx2 Bach1 Usf1 Bcl11a Rela Zfx Klf5 Onecut1 Junb Six2 Erg Tead4 Meis1 Smad4 Etv4 Maf
significance −log10
1.25
1.00
0.75
0.50
0.25
d
IL-4Rα^ΔCD8 (n=3)
H. polygyrus gavage
−d15
d0
mesLN harvest
CD8 T cells
negative selection
and FACsorting
CD124 (PE)
CD124+
CD124−
Sample Tag
and
cell pooling (ratio1:1)
BD Rhapsody cell capture
and
Sequencing
Gzmb
Ccl5
Ccr7
Il7r
Sell
Mki67
Bhlhe40
Pdcd1
Tigit
Lag3
Cxcr3
Il2rb
Expression
UMAP_1
UMAP_2

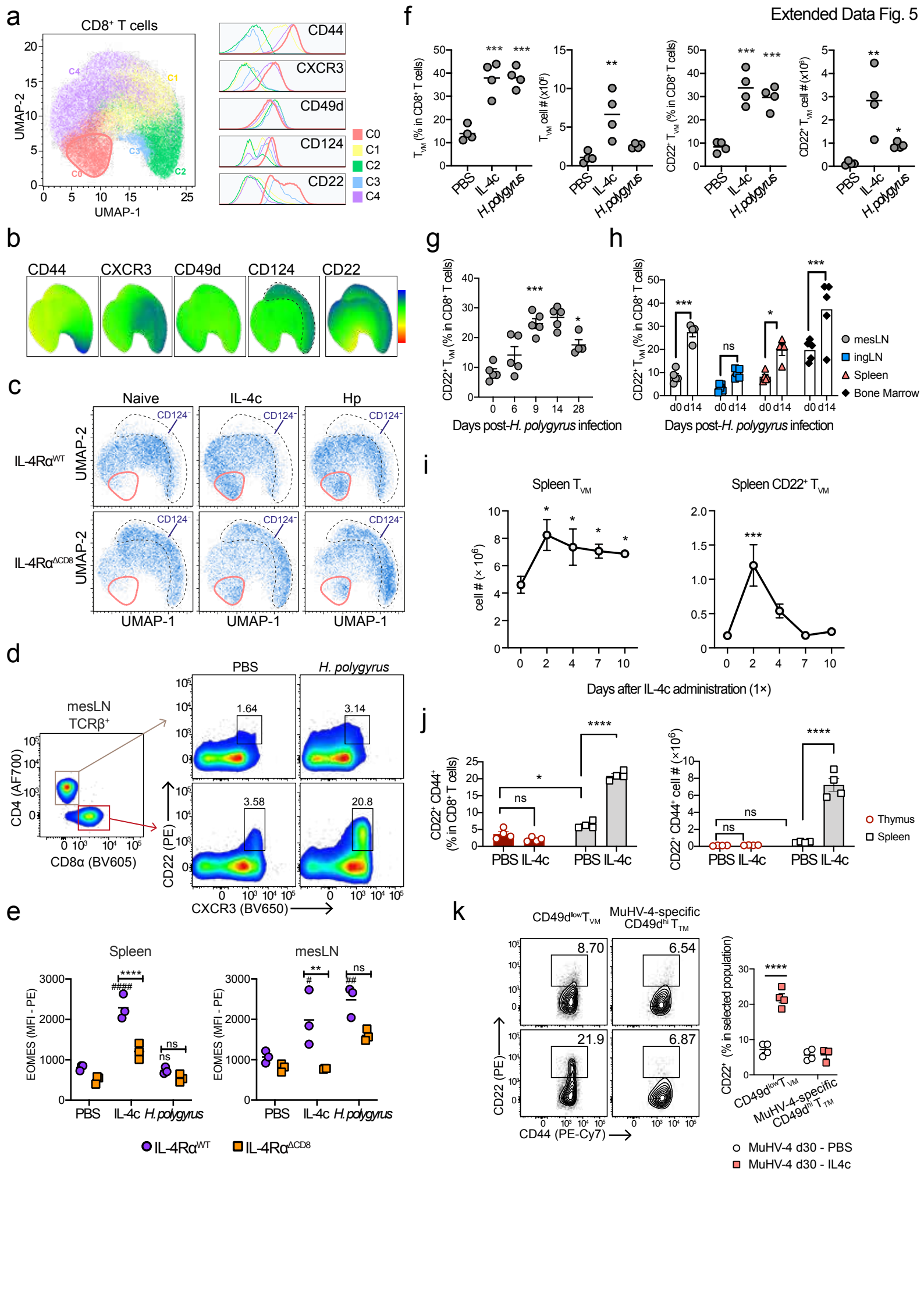
a
CD8⁺ T cells
UMAP-2
UMAP-1
C0
C1
C2
C3
C4
CD44
CXCR3
CD49d
CD124
CD22
b
CD44
CXCR3
CD49d
CD124
CD22
c
Naive
IL-4c
Hp
IL-4Rα^WT
IL-4Rα^ΔCD8
CD124⁻
UMAP-2
UMAP-1
d
mesLN
TCRβ⁺
CD4 (AF700)
CD8α (BV605)
PBS
H. polygyrus
1.64
3.14
3.58
20.8
CD22 (PE)
CXCR3 (BV650)
e
Spleen
mesLN
EOMES (MFI - PE)
PBS
IL-4c
H.polygyrus
IL-4Rα^WT
IL-4Rα^ΔCD8
f
T_VM (% in CD8⁺ T cells)
T_VM cell # (x10⁶)
CD22⁺ T_VM (% in CD8⁺ T cells)
CD22⁺ T_VM cell # (x10⁶)
PBS
IL-4c
H.polygyrus
g
CD22⁺ T_VM (% in CD8⁺ T cells)
Days post-H. polygyrus infection
h
CD22⁺ T_VM (% in CD8⁺ T cells)
d0 d14
mesLN
ingLN
Spleen
Bone Marrow
Days post-H. polygyrus infection
i
Spleen T_VM
Spleen CD22⁺ T_VM
cell # (× 10⁶)
Days after IL-4c administration (1×)
j
CD22⁺ CD44⁺ (% in CD8⁺ T cells)
CD22⁺ CD44⁺ cell # (×10⁶)
PBS IL-4c
Thymus
Spleen
k
CD49d^low T_VM
MuHV-4-specific CD49d^hi T_TM
8.70
6.54
21.9
6.87
CD22 (PE)
CD44 (PE-Cy7)
CD22⁺ (% in selected population)
MuHV-4 d30 - PBS
MuHV-4 d30 - IL4c

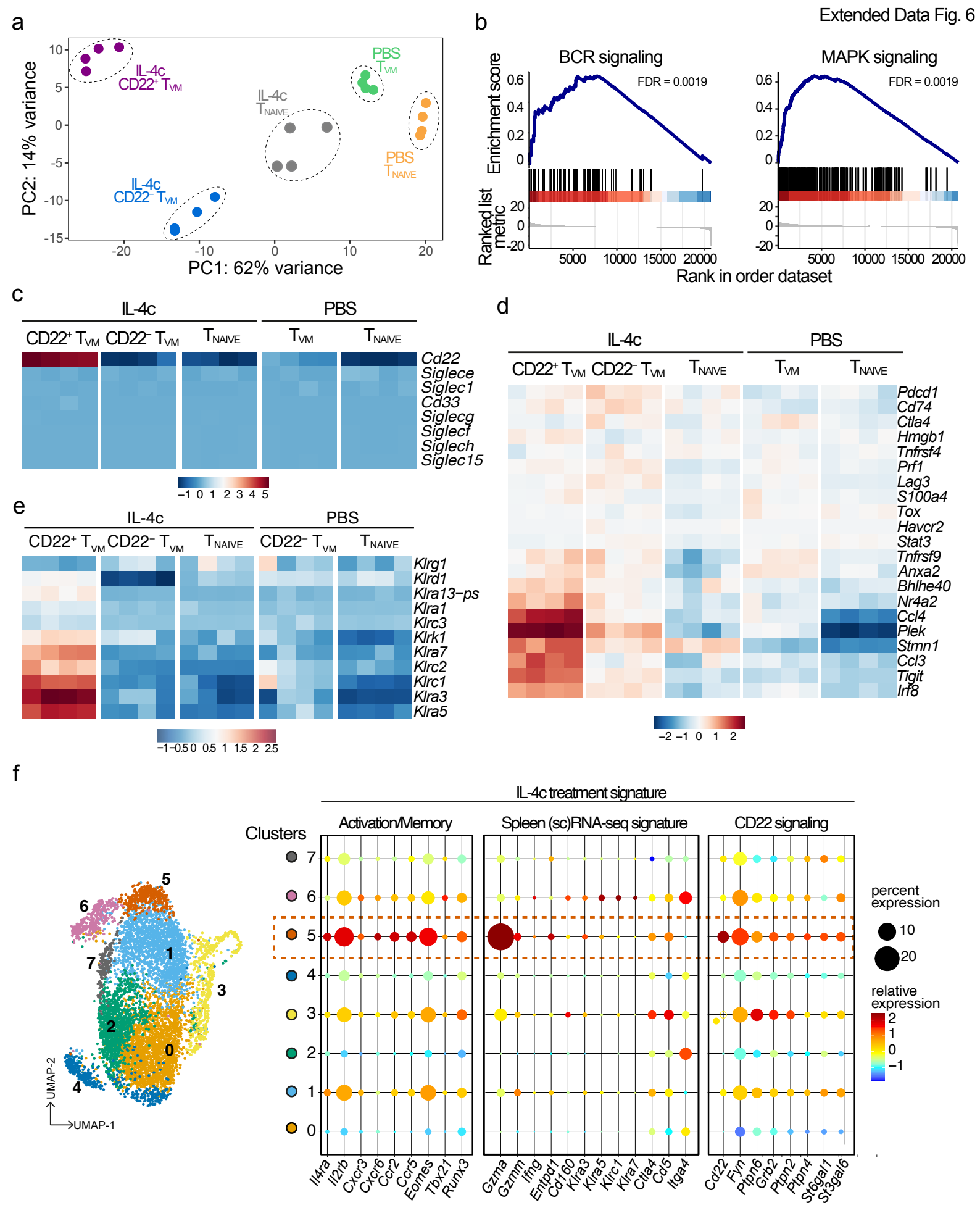
a
PC2: 14% variance
PC1: 62% variance
IL-4c CD22+ TVM
IL-4c TNAIVE
PBS TVM
PBS TNAIVE
IL-4c CD22− TVM
b
BCR signaling
MAPK signaling
FDR = 0.0019
FDR = 0.0019
Enrichment score
Ranked list metric
Rank in order dataset
c
IL-4c
PBS
CD22+ TVM
CD22− TVM
TNAIVE
TVM
TNAIVE
Cd22
Siglece
Siglec1
Cd33
Siglecg
Siglecf
Siglech
Siglec15
d
Pdcd1
Cd74
Ctla4
Hmgb1
Tnfrsf4
Prf1
Lag3
S100a4
Tox
Havcr2
Stat3
Tnfrsf9
Anxa2
Bhlhe40
Nr4a2
Ccl4
Plek
Stmn1
Ccl3
Tigit
Irf8
e
Klrg1
Klrd1
Klra13−ps
Klra1
Klrc3
Klrk1
Klra7
Klrc2
Klrc1
Klra3
Klra5
f
IL-4c treatment signature
Clusters
Activation/Memory
Spleen (sc)RNA-seq signature
CD22 signaling
Il4ra
Il2rb
Cxcr3
Cxcr6
Ccr2
Ccr5
Eomes
Tbx21
Runx3
Gzma
Gzmm
Ifng
Entpd1
Cd160
Klra3
Klra5
Klrc1
Klra7
Ctla4
Cd5
Itga4
Cd22
Fyn
Ptpn6
Grb2
Ptpn2
Ptpn4
St6gal1
St3gal6
percent expression
relative expression
UMAP-1
UMAP-2

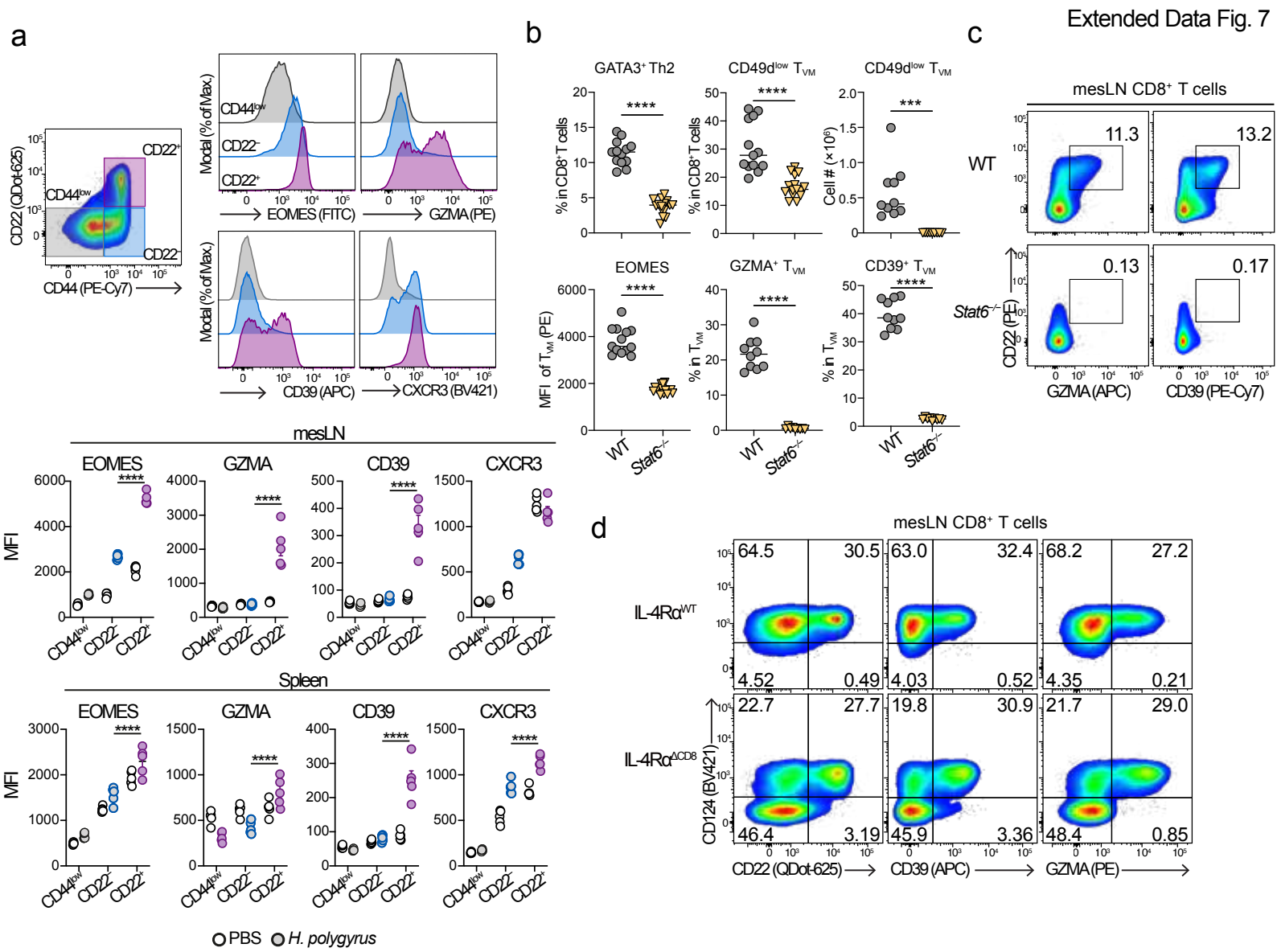
a
CD22 (QDot-625)
CD44 (PE-Cy7)
CD44low
CD22+
CD22−
Modal (% of Max.)
EOMES (FITC)
GZMA (PE)
CD39 (APC)
CXCR3 (BV421)
b
GATA3+ Th2
CD49dlow TVM
% in CD8+ T cells
Cell # (×10^6)
EOMES
GZMA+ TVM
CD39+ TVM
MFI of TVM (PE)
% in TVM
WT
Stat6−/−
c
mesLN CD8+ T cells
11.3
13.2
0.13
0.17
GZMA (APC)
CD39 (PE-Cy7)
d
mesLN CD8+ T cells
IL-4Rα^WT
IL-4Rα^ΔCD8
64.5
30.5
4.52
0.49
63.0
32.4
4.03
0.52
68.2
27.2
4.35
0.21
22.7
27.7
46.4
3.19
19.8
30.9
45.9
3.36
21.7
29.0
48.4
0.85
CD124 (BV421)
CD22 (QDot-625)
CD39 (APC)
GZMA (PE)
mesLN
Spleen
EOMES
GZMA
CD39
CXCR3
MFI
PBS
H. polygyrus

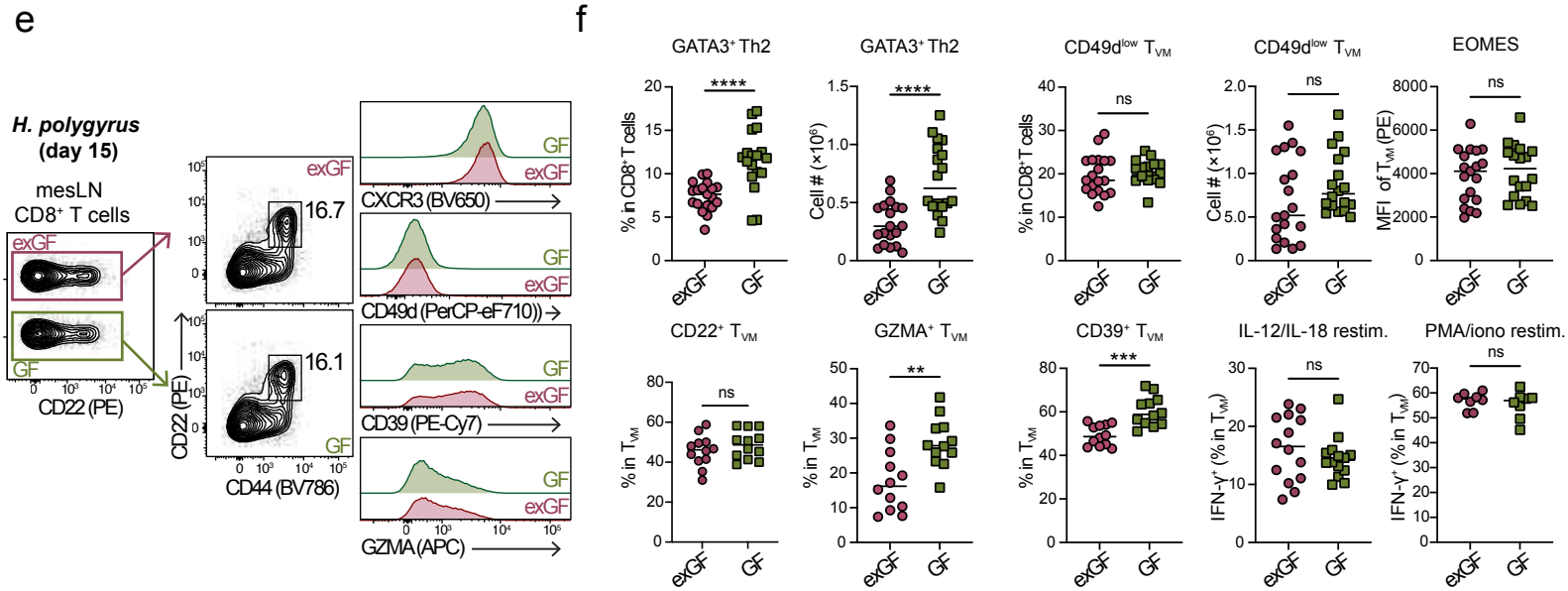
e
H. polygyrus
(day 15)
mesLN
CD8+ T cells
exGF
GF
16.7
16.1
CD22 (PE)
CD44 (BV786)
CXCR3 (BV650)
CD49d (PerCP-eF710))
CD39 (PE-Cy7)
GZMA (APC)
f
GATA3+ Th2
CD49dlow TVM
EOMES
% in CD8+ T cells
Cell # (×10^6)
MFI of TVM (PE)
CD22+ TVM
GZMA+ TVM
CD39+ TVM
IL-12/IL-18 restim.
PMA/iono restim.
IFN-γ+ (% in TVM)
ns

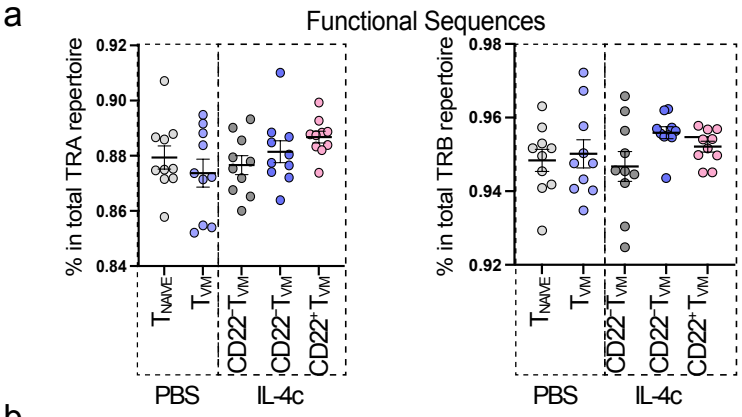

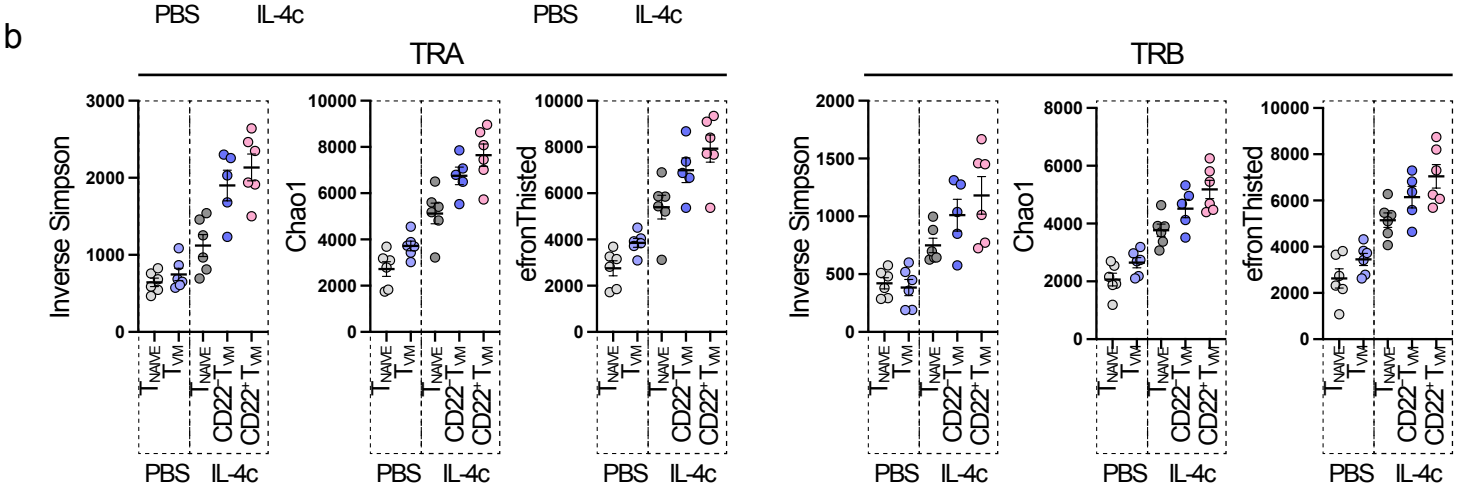

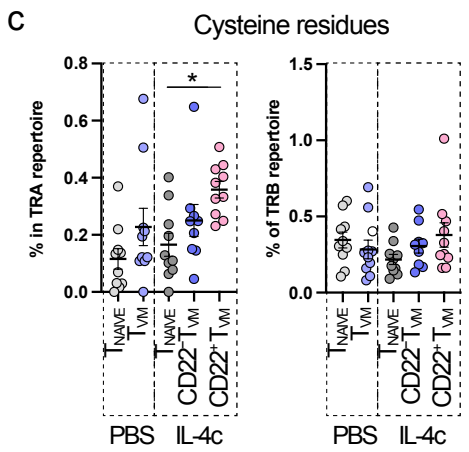

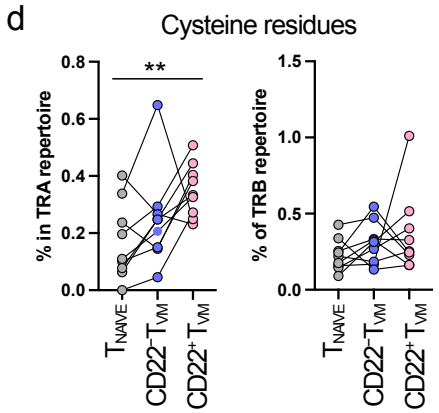

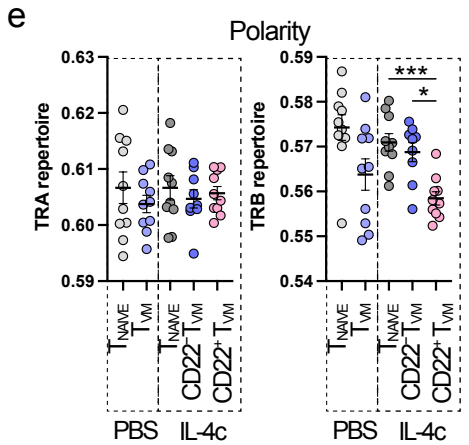

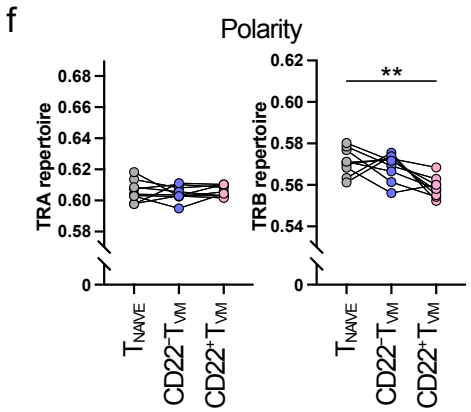

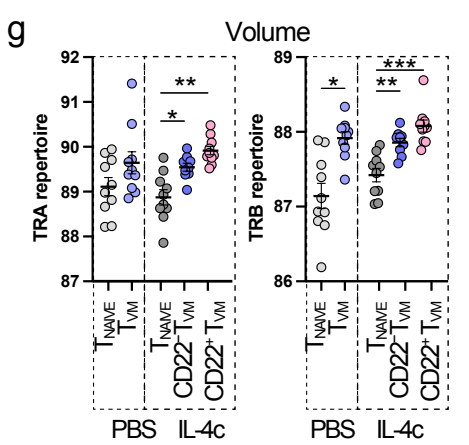

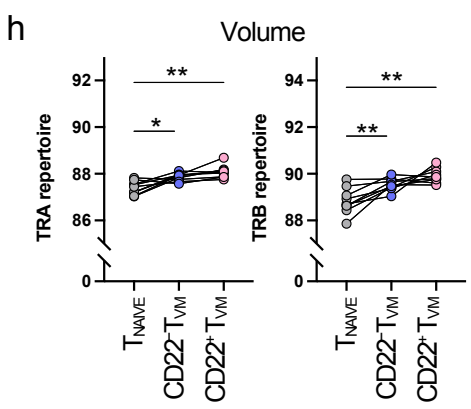

i

CDR3 physicochemical characteristics and Kidera factors used to predict self-reactive CDR3

1. polarity
2. volume
3. strength
4. mjenergy
5. charge
6. hydropathy
7. hydrophobic (H-)doublets
8. cystein (C-)residues
9. kf1: helix/bend preference
10. kf2: side-chain size
11. kf3: extended structure preference
12. kf4: hydrophobicity
13. kf5: double-bend preference
14. kf6: partial specific volume
15. kf7: flat extended preference
16. kf8: occurence of alpha region
17. kf9: pK-C
18. kf10: surrounding hydrophobicity